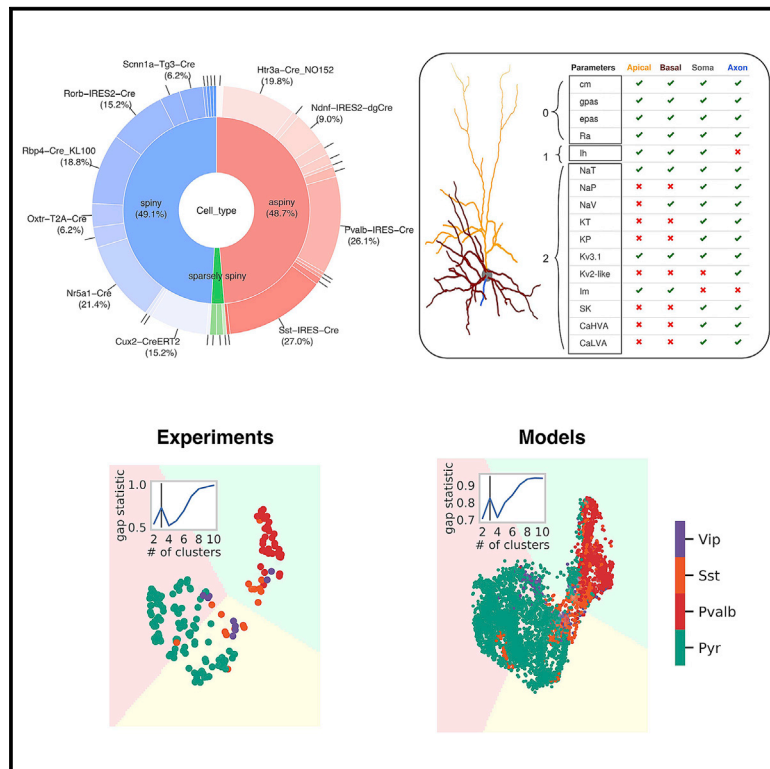


Single-neuron models linking electrophysiology, morphology, and transcriptomics across cortical cell types

Graphical abstract



Authors

Anirban Nandi, Thomas Chartrand, Werner Van Geit, ..., Christof Koch, Bosiljka Tasic, Costas A. Anastassiou

Correspondence

costas.anastassiou@cshs.org

In brief

Integrating and reconciling multimodal cellular datasets has been challenging. Nandi et al. generate models that are robust representations of cellular experiments and cortical cell types defined by electrophysiology, morphology, or transcriptomics. These models causally link between seemingly disparate modalities offering mechanistic hypotheses about cellular phenotypes.

Highlights

- 9,200 models are generated that capture multimodal single-cell datasets
- Models preserve cortical cell class relationships reproducing class differences
- Model-based conductance predictions correlate with gene expression differences
- Cell class differences in Ih translate to synaptic integration differences



Article

Single-neuron models linking electrophysiology, morphology, and transcriptomics across cortical cell types

Anirban Nandi,¹ Thomas Chartrand,^{1,8} Werner Van Geit,^{2,8} Anatoly Buchin,¹ Zizhen Yao,¹ Soo Yeun Lee,¹ Yina Wei,^{1,7} Brian Kalmbach,¹ Brian Lee,¹ Ed Lein,¹ Jim Berg,¹ Uygur Sümbül,¹ Christof Koch,¹ Bosiljka Tasic,¹ and Costas A. Anastassiou^{1,3,4,5,6,9,*}

¹Allen Institute for Brain Science, Seattle, WA 98109, USA

²Blue Brain Project, École Polytechnique Fédérale de Lausanne (EPFL), Campus Biotech, Geneva 1202, Switzerland

³Department of Neurosurgery, Cedars-Sinai Medical Center, Los Angeles, CA 90048, USA

⁴Department of Neurology, Cedars-Sinai Medical Center, Los Angeles, CA 90048, USA

⁵Board of Governors Regenerative Medicine Institute, Cedars-Sinai Medical Center, Los Angeles, CA 90048, USA

⁶Center for Neural Science and Medicine, Department of Biomedical Sciences, Cedars-Sinai Medical Center, Los Angeles, CA 90048, USA

⁷Zhejiang Lab, Hangzhou City, Zhejiang Province 311121, China

⁸These authors contributed equally

⁹Lead contact

*Correspondence: costas.anastassiou@cshs.org

<https://doi.org/10.1016/j.celrep.2022.111176>

SUMMARY

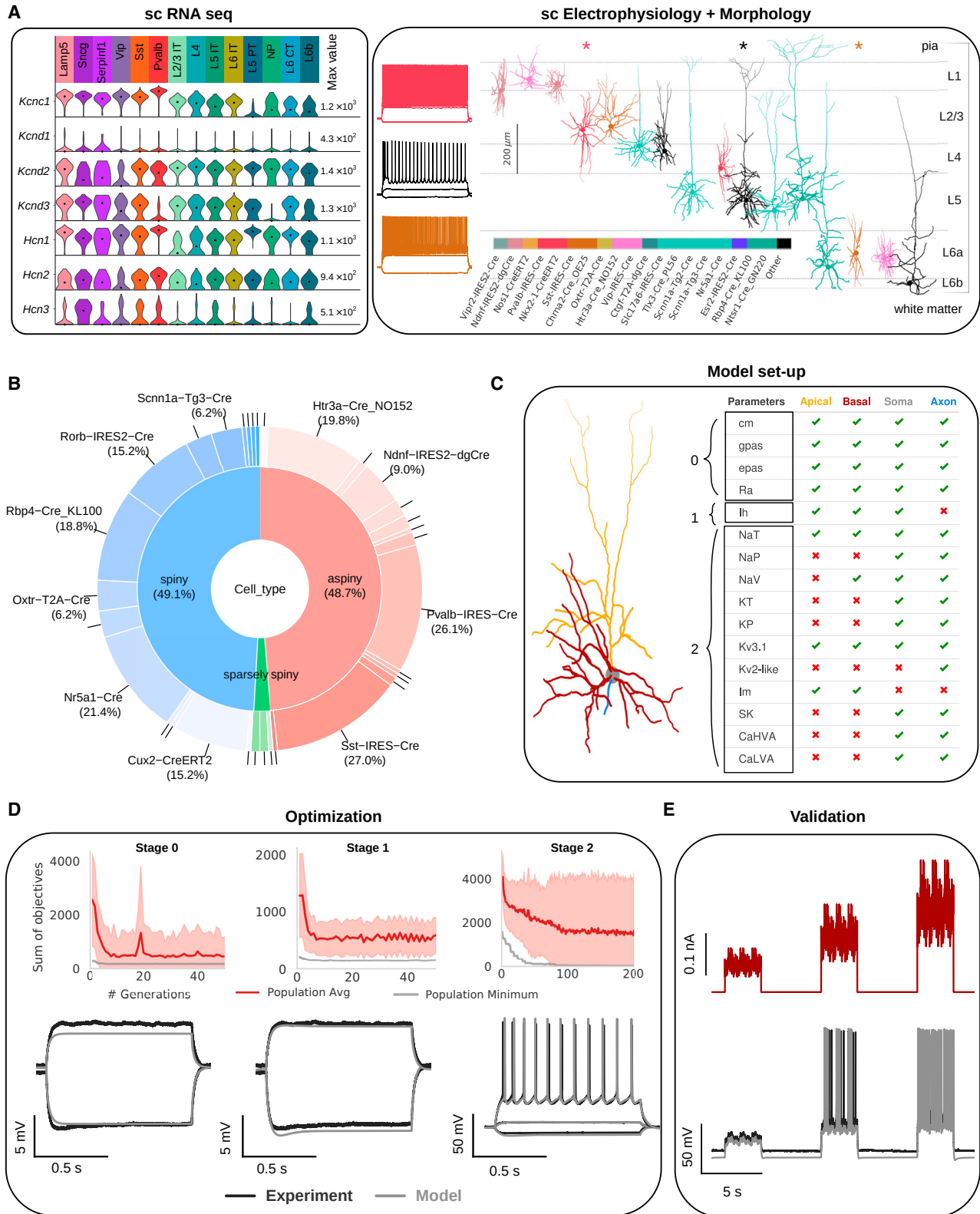
Which cell types constitute brain circuits is a fundamental question, but establishing the correspondence across cellular data modalities is challenging. Bio-realistic models allow probing cause-and-effect and linking seemingly disparate modalities. Here, we introduce a computational optimization workflow to generate 9,200 single-neuron models with active conductances. These models are based on 230 *in vitro* electrophysiological experiments followed by morphological reconstruction from the mouse visual cortex. We show that, in contrast to current belief, the generated models are robust representations of individual experiments and cortical cell types as defined via cellular electrophysiology or transcriptomics. Next, we show that differences in specific conductances predicted from the models reflect differences in gene expression supported by single-cell transcriptomics. The differences in model conductances, in turn, explain electrophysiological differences observed between the cortical subclasses. Our computational effort reconciles single-cell modalities that define cell types and enables causal relationships to be examined.

INTRODUCTION

The nervous system consists of cell classes defined by specific molecular signatures (Tasic et al., 2016, 2018a), morphologies (Markram et al., 2000, 2004), or electrophysiological properties (Gouwens et al., 2019; Hille, 1978; Lai and Jan, 2006; Prinz et al., 2003). In recent years, single-cell characterization of neurons, mainly propelled by advances in single-cell RNA sequencing (Tang et al., 2009), has revealed a multitude of “cell types” (Hodge et al., 2019; Poulin et al., 2016; Zeisel et al., 2015). Despite our ever-increasing ability to detect distinguishing molecular, morphological, and electrophysiological features to differentiate between such types, unraveling causal relationships between data modalities has been difficult. How does a particular distribution of ion channel conductances dictated by gene expression manifest itself in the various electrophysiological features recorded in slice experiments? Experimentally, this process involves elaborate genetic and/or pharmacological manipulations that are difficult to scale.

Single-cell models link various types of data by incorporating constraints and generating predictions across modalities. Two types of models have emerged: models linking transcriptomics with electrophysiology and models linking morphology with electrophysiology. While molecular and electrophysiological features can be linked via models (e.g., Prinz et al., 2003), the idea that a single model faithfully captures a particular cell has been challenged. The latter models are used to study excitability mechanisms such as spike generation and dendritic events along the neural morphology in rodents (Bahl et al., 2012; Hay et al., 2011; Mainen et al., 1995), non-human primates (Rumbell et al., 2016), and humans (Eyal et al., 2018; Kalmbach et al., 2018a; Mosher et al., 2020). A limitation is their vast parameter space that renders their generation cumbersome and computationally expensive. Hence, most studies either focus on a small number of experiments or, alternatively, models offering reduced bio-realism. It follows that *en masse* model generation has been unattainable, particularly for models linking three key experimental modalities: single-cell electrophysiology, detailed morphology, and molecular signatures.





(legend on next page)

Recently, two datasets shed light on the taxonomy of the mouse primary visual cortex. The first used single-cell RNA sequencing (RNA-seq) to define more than 100 transcriptomic cell types (Tasic et al., 2016, 2018a). The second (morphoelectric or ME-dataset) used electrophysiological responses and morphology reconstructions to define morphoelectric types (Gouwens et al., 2019). The experimental data we used to generate the single-cell models consisted of a “broad” taxonomy comprising four major subclasses (vasoactive intestinal peptide [Vip], somatostatin [Sst], parvalbumin [Pvalb], and pyramidal [Pyr]) and seven “refined” subclasses—three GABAergic (Vip, Sst, and Pvalb) and four glutamatergic (L2/3 IT, L4, L5 IT, and L5 PT).

We develop a model generation workflow to make biologically faithful single cells for 230 excitatory and inhibitory single cells. This large-scale optimization effort results in a set of ion channel conductance values for each morphology section (soma, axon initial segment, and apical and basal dendrites). We use the “all-active” models to address three important questions: Do the models represent cortical classes and subclasses by capturing key features and divergent properties between these populations? Can the models explain distinguishing properties between cell subclasses across data modalities? How unique are the all-active model representations? We show that the models recapitulate the unique features of major excitatory and inhibitory cell classes across modalities. We use the ion channel conductance vectors to formulate specific, model-based predictions for differentially expressed ion channels. For a subset of excitatory and inhibitory cell classes, we show that the model-based predictions are confirmed by transcriptomics. Given that the models are trained on electrophysiology and morphology data (and not on transcriptomics), this is an emergent property of the model generation procedure. These differentially expressed genes directly manifest themselves in distinct, cell-type-specific electrophysiology properties separating cell classes.

RESULTS

Large-scale generation of single-cell models

The excitatory and inhibitory neurons originate from mouse primary visual cortex (V1 or VISp) and neighboring cortical areas across six cortical layers (Figure 1A). We used two data sets: (1) a single-cell transcriptomics set in which gene expression is

quantified in counts over million reads (Tasic et al., 2016, 2018a) and (2) a single-cell patch-clamp electrophysiology and reconstructed morphology set (Gouwens et al., 2019). Both studies used transgenic Cre lines for targeting (Daigle et al., 2018). For each of the 230 single-cell experiments considered here, we accounted for soma location with respect to cortical layer (L1–L6) and dendrite morphology type (“spiny,” “aspiny,” “sparsely spiny”). Cre lines are grouped into 4 “broad” subclasses: The Pyr subclass represents all excitatory Cre lines (Pyr; see STAR Methods) and three inhibitory subclasses expressing Pvalb, Sst, or Vip (Gouwens et al., 2019) (Figures 1A and 1B). Throughout the manuscript, we use the nomenclature introduced above—in other words, cell classes characterize the excitatory and inhibitory divide based on the morphology type, and any data-driven subdivision of these two classes is denoted as a subclass (Figure S1).

We generate the all-active models from the electrophysiology response and the reconstructed morphology of the same neuron. The main challenge lies in distributing active conductances along the morphology (Figure 1C) in a way that the model replicates the experimental electrophysiology features (“E-features”). The passive properties, together with the maximal conductances (\bar{g}) for the voltage-gated Na^+ , K^+ and Ca^{2+} - channels, are represented with a vector that uniquely identifies every model. Fitting the conductances requires formulating a multi-objective optimization (Miettinen, 2012), in which each objective measures the distance between the experimental and model features for the specific current input (direct current [DC] steps) (Druckmann et al., 2007, 2011). The optimization leverages evolutionary algorithms (Fortin et al., 2012; Van Geit et al., 2016), continuously seeking to improve the previously evaluated solutions. We developed an automated workflow that divides the fitting procedure in three stages: passive parameter fit (stage 0), h-channel conductance density fit (stage 1), and all-active parameter fit (stage 2; Figure 1C; STAR Methods). The multi-objective optimization aims to reduce each objective independently (Figure 1D), resulting in the fit for a set of E-features (Tables S2 and S3). To validate each all-active model, we evaluated it on novel (i.e., not included in the training/optimization) current stimuli (noise stimuli) that models did not train and compared features against experimental data from the same noise stimuli (Figure 1E).

We used 15 models of voltage-gated ion channels (Table S1) known to be expressed in rodent cortical neurons (see STAR

Figure 1. Cell types in mouse visual cortex (VIS) and single-cell model generation

- (A) Data modalities: single-cell transcriptomics (left) (Tasic et al., 2016), (right) single-cell morpho-electric (ME) data (Gouwens et al., 2019). Sample morphologies arranged according to normalized depth from pia, including putative cortical layer markings and electrophysiological recordings for 3 cells in the same set under subthreshold and suprathreshold current injections (colors: Cre line).
- (B) Overview of the 230 modeled cells in the ME dataset based on dendrite type and Cre line (cell class— spiny: putative excitatory, sparsely spiny, and aspiny: putative inhibitory). See also Figure S1.
- (C) Model setup: Morphology (CellID: 483101699) and a predefined set of active conductances/passive properties marked according to their inclusion in each morphology section (apical, basal dendrites, soma, AIS).
- (D) The 3-stage optimization workflow (stages 0, 1, 2). The parameters added to the variable list at each stage are highlighted in (C) (table, left). (Top) Evolution of the sum of objectives with generation number. The best model (gray) at each generation and the average performance of all of the individual models (red) of that generation (spread: standard deviation of the population). (Bottom) Comparison between experimental traces (black) and the fitted model (gray) at each stage for a representative model (same as in C).
- (E) Validation comprising novel stimulation protocols (top; noise stimulation) and comparison between model and experiment spiking responses (bottom) under the novel noise stimulus (i.e., standardized colored noise [top]) to evaluate explained variance (see STAR Methods).

Methods; Gouwens et al., 2018; Hay et al., 2011), kept their kinetic parameters unaltered, and only allowed \bar{g} and the passive properties to vary. This resulted in a maximum of 43 variables per model along four identified regions of the morphology (soma, axon initial segment [AIS], and basal and apical dendrites). To optimize these variables for a single all-active model, the workflow involved 300 generations (stage 0: 50, stage 1: 50, stage 2: 200), with 512 new models generated and evaluated at each generation. The final model was selected from a group of 10 best models generated in this evolutionary procedure (termed “hall of fame” [HOF]) for a single seed. Four seeds were used to randomize initialization from the same parameter bounds. In total, a single all-active model required the generation and evaluation of more than 600,000 models. Therefore, model generation for the entirety of the single-cell experiments required the evaluation of more than 130 million single-cell models and 3.5 million central processing unit (CPU) core hours.

Models of major cortical cell types: Uniqueness and within versus across cell-type variability

Model quality is assessed by the extent to which the properties of a particular neuron or cell type are captured. Classes separable via a particular electrophysiological, morphological, or transcriptomic property should lead to models separable by the same property. The experimental data used to generate the models consist of a “broad” taxonomy comprising four major subclasses (Vip, Sst, Pvalb, and Pyr). Seven transcriptomic cell subclasses (Gouwens et al., 2019) had enough experiments across modalities; this group formed a “refined” taxonomy: 3 GABAergic (Vip, Sst, and Pvalb) and 4 glutamatergic (L2/3 IT, L4, L5 IT, and L5 PT).

How well do all-active models capture experimental E-features? We calculated the Z score for each feature in the best model from the optimization process (see STAR Methods), with the error for the entire training set across models being typically less than 2 standard deviations from the experimental values. Features such as resting potential, spike amplitude, time-to-first spike, and spike frequency were captured particularly well (Figure S2). To test the optimization workflow against ground truth, we also ran cases recovering model parameters

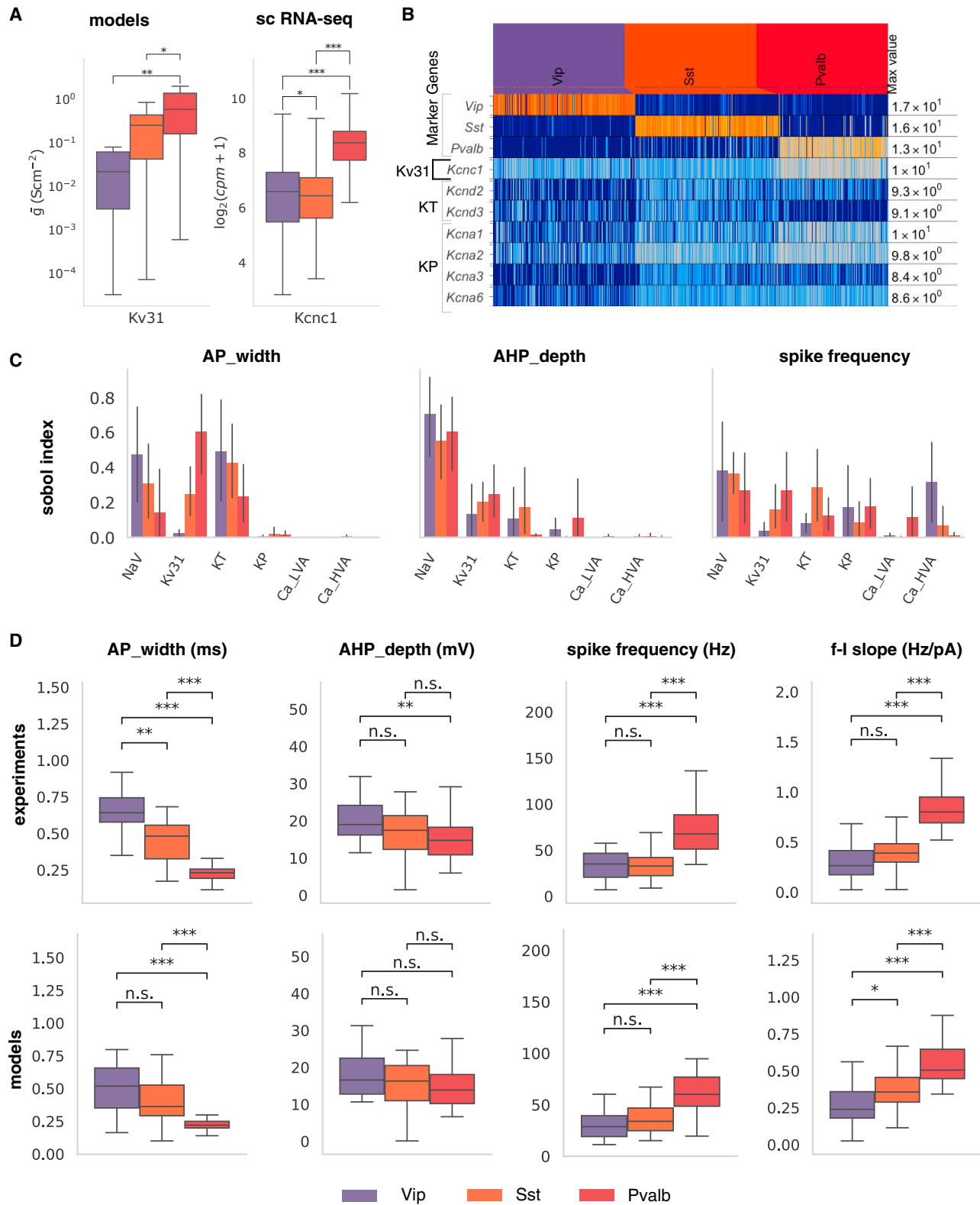
and E-features starting from a fitted input model (Figure S3). Despite the vast parameter space and randomized initialization, the conductances of the re-optimized models converged to the values of the original models (Figure S3).

Typically, a single model is developed for a single-cell experiment. However, generating conductance-based models from E-features is ill-posed (Prinz et al., 2003). We looked beyond the best model of the optimization and instead took the 40 best models exhibiting the smallest sum of objectives (HOF models) out of the optimization workflow (Van Geit et al., 2016). These HOF models are representations of the E-features of a single-cell experiment given a reconstructed morphology, constituting the group of best models out of more than 600,000 models evaluated during the optimization. How much better does the best model perform over its HOF counterparts? A substantial decrease in model performance would point to the best model representing a unique and near-optimal solution in the parameter landscape. Instead, HOF models exhibit a graded increase in the training set error (Z score; Figure S4) and perform equally well (in terms of explained variance, see STAR Methods) for noisy stimulation they were not trained on (Figure S4). Therefore, while the best model of an experiment represents a solution with the smallest training error, the 39 other HOF models generalize equally well in two different types of stimulation sets irrespective of their initialization. This points to a single experiment reflected in a family of models with similar performance rather than a single, optimal one.

We hypothesized that the existence of multiple conductance vectors for a single cell can inform on cell-type representation across data modalities. We looked closer into HOF conductance dispersion and measured it within experiment (HOF) versus across a cell class: If conductance variability of HOF models is larger than conductance variability across models of the same cell class, it would be difficult to associate between conductance vectors and cell-type identity (Figure 2A). Despite variability, the conductance vectors in HOF models for a particular experiment exhibit significantly smaller dispersion than across any of the four major cell classes (Figures 2A and 2B and S5). To validate that these global cross-class relationships are also consistent in the space of E-features, we compare the clustering structure in

Figure 2. All-active models conserve decision boundaries and cross-class relationships of experimental features that reproduce key differences within and between cell classes

- (A) Left: The parameters across the 40 hall of fame (HOF) models corresponding to each cell creates a cluster in \bar{n} -dimensional euclidean space (\bar{n} : common parameters across all cells). The centroid of this cluster (color: euclidean distance between HOF index and its centroid). The sum of all distances measures cluster dispersion (bar plot top of the distance matrix). (Right) t-Distributed stochastic neighbor embedding (t-SNE) plot highlights 4 cases of maximally (red: excitatory cell; green: inhibitory cell) and minimally (blue: excitatory cell; magenta: inhibitory cell) dispersed parameter vectors in 2 dimensions (2D).
- (B) Left: Heatmap showing euclidean distances between HOF models for the 3 broad inhibitory classes; each block diagonal represents 40 HOF models for a single cell. Right: Interpretation for different regions of the heatmap, namely, intracell intraclass (blue), intercell intraclass (orange), and intercell interclass (green). Darker block diagonals and the distribution of the intra/inter distances for the 3 broad classes indicate an ordered structure in the parameter dispersion. Degenerate parameters for a single cell are tightly clustered compared to parameters of the same broad class followed by model parameters between different classes ($p < 0.01$; Mann-Whitney U test).
- (C) For cells belonging to the 4 broad subclasses, HOF model E-features at the maximal amplitude stimulus protocol and projected onto UMAP embedding of the corresponding features at the experiment level (optimal number of clusters: $n_{\text{clusters}} = 3$ via gap statistic (Tibshirani et al., 2001)). The corresponding k-means decision boundary is drawn on the embedded space for the experiment, the best model (HOF index = 0), and all HOF models (40 models per cell). The number of detected clusters, their composition, and associated decision boundaries remain unaltered.
- (D) UMAP embedding of HOF parameters colored according to the broad subclasses.
- (E) Similar to (D), the separation in the electrophysiology and model parameter space is also preserved between two putative excitatory types, namely L2/3 and L5 PCs.
- (F) The separation in the HOF model parameter space between two excitatory L5 excitatory types, IT and PT.



(legend on next page)

this space between experiments, best model, and HOF population. The clusters detected using experimental E-features (Figure 2C, left) are conserved when using the same features from the best model (Figure 2C, center). When features from the HOF models are accounted for (40 models per experiment; in total: $230 \times 40 = 9,200$ models evaluated), the number of clusters and, more important, decision boundaries agree between experiments, best model, and HOF models (Figure 2C, right). We conclude that both the best models and the HOF population of the all-active models conserve decision boundaries as well as cross-class relationships of experimental E-features. By doing so, they reproduce key convergent properties within cell classes as well as divergent properties between them.

To what extent do these models represent major cortical subclasses? We clustered the conductance vectors of all models (including the HOF population) and saw that the model parameters cluster accordingly between major cortical populations into one excitatory (Pyr) and three inhibitory (Vip, Sst, and Pvalb) subclasses (Figure 2D; see STAR Methods). In terms of experimental and model features (both best model as well as HOF), the populations of the different subclasses remain coherent. For example, Pvalb cells are adjacent to Sst, while Vip are on the other side of the Sst cells. Notably, these markers label largely mutually exclusive subclasses of interneurons (Tremblay et al., 2016; Tasic et al., 2016; Gouwens et al., 2019). We conclude that uniform manifold approximation and projection (UMAP) embedding separation is seen not only for experiments but also for best model and HOF E-features pointing to distinct ion conductance patterns between the cell classes.

While inhibitory cell types tend to be well separated, excitatory cell types exhibit more pronounced overlap and within-type diversity, especially in terms of E-features and transcriptomics (Gouwens et al., 2019; Tasic et al., 2016). A robust differentiator of excitatory cells is the cortical depth of their soma location separating two distinct populations, superficial versus deep excitatory cells (Tasic et al., 2016). We tested whether this separation is also observed in our data and found it is for experiment and HOF model E-features, but, notably, also for model parameters (Figure 2E).

Another prominent division is between L5 excitatory neurons, namely between L5 intratelencephalic (IT) versus extratelencephalic (often called pyramidal tract, or PT) Pyr neurons. Both send axonal projections within the telencephalon, but only PT neurons send long-range axons to subcerebral targets. Importantly, PT neurons possess distinct morphoelectric and gene expression properties over their IT counterparts (Anastasiades et al., 2018; Brown and Hestrin, 2009; Dembrow et al., 2010; Hat-

tox and Nelson, 2007; Kawaguchi, 2017; Kim et al., 2015; Sorensen et al., 2015; Tasic et al., 2018b). We tested whether the all-active models also reflect this division. We looked within the L5 Pyr population by separating IT and PT neurons based on marker genes (Deptor, Slc30a3) and found that conductance vectors between L5 IT and PT HOF models separate despite some overlap (Figure 2F). While L5 PT conductance vectors resemble more (and thus are closer to) those of superficial excitatory neurons, L5 IT conductance vectors are more distinct (Figure 2F). This observation is consistent with studies reporting that IT neurons are distinct (Gouwens et al., 2019). We conclude that the generated models recapitulate salient E-features of major cortical cell classes and subclasses that separate between distinct excitatory and inhibitory populations. Moreover, the conductance vectors generated by the all-active optimization workflow reflect distinct compositions of cell subclasses that conserve the relationship between cortical subclasses.

From electrophysiology to gene expression: Model predictions and experimental validation

The all-active models are optimized on E-features and morphological reconstructions. Do models reflect the transcriptomic signatures of the cell class or subclass they represent (e.g., can conductances predict the expression of specific ion channel genes)? We looked in the three inhibitory subclasses represented by intersection of Cre lines Vip, Sst, and Pvalb and morphology in the single-cell RNA-seq dataset (Tasic et al., 2016) (filtered for basket cells in Pvalb and neuroglia Vip cells; see STAR Methods). When looking at the differentiating genes, the ion channel-related genes or the ion channel-related genes of conductances included in our models between the subclasses, it is neither possible to determine meaningful differences nor to predict how gene-based differences will materialize in terms of E-features *a priori* (Figure S6).

We ran pairwise comparisons between the 15 somatic ion channel conductances. The comparison in inhibitory somatic conductances reveals that the Kv3.1 conductance is significantly different between models of the three inhibitory types (Figure 3A): Kv3.1 conductance increases from Vip to Sst to Pvalb, with Vip exhibiting the lowest and Pvalb the highest Kv3.1 conductance between the three subclasses. Motivated by these model-based predictions, we looked at the expression profile of K^+ conductance-related genes, namely, *Kcnc1*, *Kcna1-3*, *Kcnd1-3* associated with Kv3.1, persistent K^+ (KP), and transient K^+ (KT) conductances, respectively. For *Kcnc1*, which encodes Kv3.1 (Muona et al., 2015; ; Wymore et al., 1994), there is agreement between the experimentally measured differential

Figure 3. Model-based prediction in Kv3.1 differences between GABAergic cell classes are supported by single-cell RNA-seq and explain divergent electrophysiology properties

(A) Comparison between single-cell model, somatic ion channel conductance profiles, and single-cell expression of associated genes via single-cell RNA-seq for Kv3.1 (associated gene: *Kcnc1*); boxplot: median, 1.5 interquartile range; cpm, counts per million.

(B) Expression profiles of marker genes (*Pvalb*, *Sst*, *Vip*) and specific ion channel (Kv3.1, KP – persistent K and KT – transient K) genes (*Kcnc1*, *Kcna1-3*, *Kcnd1-3*, respectively) for a set of GABAergic lines in mouse V1 via single-cell RNA-seq.

(C) Ion channels predicted by the models and confirmed by sequencing to differentially express between inhibitory cell types affect E-features. Sensitivity analysis of single-cell models (line: mean; error bar: 95% confidence interval).

(D) Top: Analysis of E-features from *in vitro* experiments. Bottom: Class-specific characteristics are preserved in the corresponding all-active models, providing a validation step for the ion channel predictions (boxplot, circles: single-cell data). Statistical testing: Mann-Whitney *U* test; statistical significance: * $p < 0.05$, ** $p < 10^{-2}$, *** $p < 10^{-3}$, adjusted for a false discovery rate (FDR) of 5%.

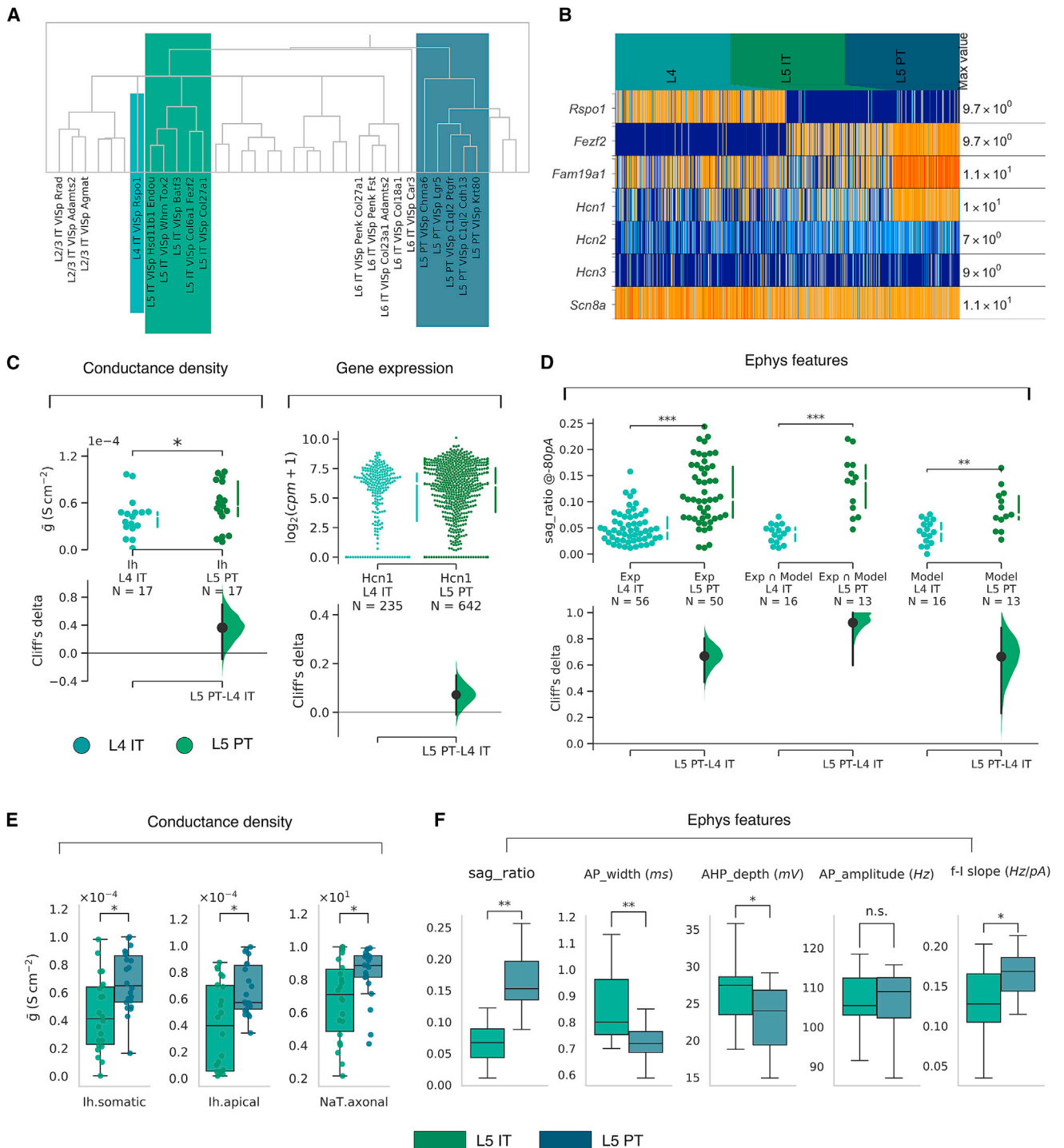


Figure 4. Model-based predictions in Ih and NaT differences between 3 excitatory subclasses link transcriptomic and electrophysiological properties

(A) The 3 excitatory subclasses L4 IT, L5 IT, and L5 PT highlighted in the transcriptomic tree derived from single-cell transcriptomics (Tasic et al., 2016). (B) Gene expression of the top differentially expressed (marker) genes between the 3 excitatory subclasses (Rspo1, Fezf2, Fam19a1) and ion channel genes implicated by the model-based predictions via pairwise comparisons: Ih (HCN1-3) and transient Na (Scn8a) (heatmap). (C) Left: h-Channel conductance density comparison between Nr5a1 (L4 IT) and L5 Rbp4 (L5 PT) models ($p < 0.05$, 1-sided Mann-Whitney U test; Cliff's delta effect size analysis of the medians (Ho et al., 2019). Right: Same comparison for gene expression from the single-cell transcriptomics between Nr5a1 (L4 IT) and L5 Rbp4 (L5 PT).

(legend continued on next page)

expression and the model prediction between the three inhibitory subclasses (i.e., Vip < Sst < Pvalb; Figure 3B). Importantly, the constraints for all of the conductances in the optimization of the inhibitory models were identical and initialization randomized (see STAR Methods). We conclude that for the inhibitory subclasses considered here, ion channel conductance vectors inferred from the E- and morphology features are consistent with differential expression patterns for these subclasses (i.e., the conductance vectors also reflect a data modality they did not train on, single-cell transcriptomics).

We then asked whether the differences observed in conductances can explain the divergent E-features between the inhibitory subclasses. Notably, assessing the influence of individual AIS or somatic conductances on a particular E-feature is non-trivial, as relatively small differences can significantly affect model response (Figure S7). To disentangle the role of individual conductances on the E-features, we used polynomial chaos expansions that allow uncertainty quantification and sensitivity analysis to be performed on single-cell models (Tennøe et al., 2018). The analysis results in a Sobol index per conductance that represents its contribution to the variability of the E-feature. The Sobol index ranges from 0 to 1, with 0 indicating no contribution of a conductance to a particular E-feature while 1 translates to that conductance explaining all variability with no others contributing. We assessed the impact of 6 somatic conductances (3 of them K⁺ related) on action potential (AP) width, after hyperpolarization (AHP) depth and spike frequency (Figure 3C). These three E-features were selected as they have been linked to Kv3.1. Models predict that Kv3.1 significantly affects the AP width together with the voltage-gated Na⁺ conductance (Nav) and KT. The AHP depth is mostly affected by the Nav and, more weakly, by the Kv3.1 conductance, with Nav mostly influencing Vip neurons. Spike frequency is affected by a spectrum of conductances in varying degrees. These results agree with experiments showing the role of Kv3.1 on high-frequency firing (Erisir et al., 1999; Lien and Jonas, 2003; Rudy and McBain, 2001), modulation of spike shape (especially narrow spike width and fast AHP; McMahan et al., 2004; Mehaffey et al., 2008; Porcello et al., 2002), as well as differential expression of Kv channels between Pvalb and Sst subpopulations (Chow et al., 1999). Despite the highly nonlinear relationship between conductances and resulting E-features, pairwise conductance comparison between all-active models reveals the role of conductances (primarily Kv3.1 but also KT) in shaping the differences in three E-features (AP width, AHP depth, spike frequency) between three inhibitory subclasses.

Cross-class conductance differences should lead to differences in E-features between classes, with each subclass, in principle, possessing a unique electrophysiological signature across a set of related features. Experimentally, pairwise comparison of E-features differentiates the three inhibitory sub-

classes: Pvalb exhibits characteristically tight AP waveforms (AP width, AHP depth) and rapid firing (spike frequency, spike frequency-current or f-I relationship) while Vip exhibits wider AP waveform and slower firing resembling excitatory neurons (Figure 3D, top row). The model simulations performed under identical conditions as patch-clamp experiments (i.e., DC stimulus amplitude and duration; Figure 3D, bottom row) agree with the experimental data, with absolute values of the E-features as well as between-class relationships conserved between experiments and models. For example, the relationship for the AP width (Δt) is conserved ($\Delta t(\text{Pvalb}) < \Delta t(\text{Sst}) < \Delta t(\text{Vip})$) between experiments and models, with Pvalb exhibiting the smallest AP width (median, interquartile range; models: 0.22, 0.05 ms; experiments: 0.23, 0.06 ms), then Sst (models: 0.36, 0.23 ms; experiments: 0.42, 0.16 ms) and, finally, Vip (models: 0.52, 0.30 ms; experiments: 0.63, 0.31 ms). Similar observations are made for AHP depth, spike frequency, and f-I slope. We conclude that the single-cell models of three inhibitory subclasses (1) link electrophysiology and morphology data (model training set) to specific conductance profiles they did not train on, predicting the expression profile of specific ion channel genes as measured by single-cell RNA-seq, (2) link conductances differentiating between the major inhibitory subclasses with key E-features that also separate these subclasses, and (3) capture between-class differences as well as within-class variability as measured experimentally.

Next, we asked what all-active models of excitatory subclasses can say about differences in conductance levels and to what extent these differences can explain divergent subclass-specific E-features. We looked at glutamatergic IT versus PT neurons and three distinct subclasses, L4 IT, L5 IT, and L5 PT neurons (Figures 4A and 4B). Comparing the differentiating genes, the ion channel-related genes or the ion channel-related genes of conductances included in our models between the excitatory subclasses, it is impossible to determine meaningful differences and predict how gene-based differences will manifest on E-features *a priori* (Figure S6). Specifically for L4 IT versus L5 PT neurons, pairwise comparison across conductance vectors of L4 IT versus L5 PT models shows a statistically significant difference in lh, with L5 PT models exhibiting an elevated lh conductance over the L4 IT models. Informed by the model-based prediction, we compared the gene expression in the single-cell RNA-seq data between Nr5a1 (L4 IT) and L5 Rbp4 (L5 PT) cells and found that expression agrees with the model conductance trend (i.e., L5 PT cells exhibit elevated HCN1 expression compared to L4 IT cells) (Figure 4C). We then asked whether this variation can explain differences in the electrophysiology between L4 IT and L5 PT neurons. The E-feature linked to lh is the sag response to a hyperpolarizing current injection (Hogan and Poroli, 2008; Kalmbach et al., 2018a). Looking at sag_ratio (Table S2), L5 PT cells exhibit significantly larger sag

(D) Analysis of sag in the E-responses. Sag_ratio (Table S2) comparison at -80 pA between (left) all cells of the two Cre lines, (center) the subset of experiments for which models were generated, and (right) the corresponding model responses.

(E) Pairwise comparison between L5 IT and PT models reveals elevated somatic, apical h channel, and transient axonal Na conductance density for L5 PT cells (with the same Hcn1, Scn8a expression pattern between the 2 classes; line, mean; error bar, 95% confidence interval)

(F) Experimental E-features comparison between L5 IT and PT cells (line, mean; error bar, 95% confidence interval). Statistical testing: Mann-Whitney U test; statistical significance: *p < 0.05, **p < 10⁻², ***p < 10⁻³, adjusted for a false discovery rate (FDR) of 5%.

response than L4 IT for all of the experiments as well as the subset of the modeled cells (Figure 4D). Also, when looking at the models, we also see a sag response significantly more pronounced for L5 PT than for L4 IT models, a result of their increased Ih conductance. We conclude that the all-active models reflect the h-channel differences observed between excitatory subclasses via single-cell RNA-seq (without being trained on this dataset at any point), while also tying the Ih conductance to E-features that distinguish between the subclasses such as the sag response.

We also looked at L5 IT versus PT cells, two distinct populations in terms of cellular properties as well as conductance vectors (Figure 2F). Pairwise comparison reveals a significantly higher somatic and apical Ih conductance as well as transient axonal Na conductance for L5 PT versus IT models (Figure 4E). The gene closest related to NaT is Scn8a, which encodes transient axonal Na conductance (Goldin et al., 2000; Katz et al., 2018; Raman et al., 1997). Comparing NaT conductance and Scn8a expression, we found agreement in the effect direction as well as statistical significance, with L5 PT exhibiting elevated NaT conductance and Scn8a expression compared to IT neurons (Figure S8). We then compared experimental E-features between L5 IT and PT neurons and found evidence in support of the conductance differences. Beyond the pronounced sag_ratio of L5 PT neurons explained by their elevated Ih, we also found that L5 PT neurons exhibit a decreased AP width and an increased f-I slope over IT neurons, even if their AP amplitude is similar (Figure 4F). This E-feature pattern can be explained by an increased transient Na conductance along the axon initial segment of L5 PT neurons (Katz et al., 2018; Noujaim et al., 2012; Raman et al., 1997; Royeck et al., 2008; Sittl et al., 2011). We summarize that the all-active models capture key properties of excitatory subclasses (L4 IT, L5 IT, and L5 PT), offering a statistical way to link transcriptomics with divergent E-features via specific ion conductances (in this case, Ih and NaT).

How are the differences observed between subclasses manifested in their ability to process information in the brain? Synaptic input *in vivo* occurs along the extended neuronal morphology. Superficial (layer 2/3 or L2/3) versus deep (L5) Pyr neurons are distinct in E-features (Figure 2E). Further analysis and pairwise comparison of the conductance vectors reveals a statistically significant difference only in the Ih conductance between L2/3 and L5 Pyr models, with elevated Ih observed along the dendrites of L5 models (Figure 5A). We tested this model-based prediction on the single-cell RNA-seq dataset and found that, indeed, pairwise comparison of the differential expression in HCN1-3 exhibited elevated expression of HCN1 in deep versus superficial Pyr neurons (Figure 5A).

To test how synaptic integration is affected by Ih, we set up simulations placing synapses along the apical dendrites of the two subclasses, activated them individually, and measured the somatic postsynaptic response (Figure 5B). We looked at the change in excitatory postsynaptic potential (EPSP) properties for two scenarios: a “dendrite-only” versus a “soma-only” synaptic activation scenario—in other words, by using the same temporal synaptic activation but changing the location of the impinging synaptic input from dendritic (dendrite-only) to purely somatic (soma-only) (Figure 5C). Importantly, both sce-

narios were instantiated along the same reconstructed morphology. Next, we compared the somatic responses between L2/3 and L5 Pyr models to find cross-class differences in the somatic EPSP response (Figure 5D). The trends we report are not morphology specific as somatic response comparison is always done in the same morphology for soma-only versus dendrite-only input. While L2/3 versus L5 Pyr morphologies differ, the measure we chose looks at the relative effect for a given morphology and then compares trends between the two cell classes. Comparison between dendritic versus somatic synaptic input shows that deep neurons exhibit smaller change in somatic postsynaptic response amplitude, width, and latency compared to when the synaptic input is directly injected into the soma (Figure 5D). This trend was robust across cases and apical distances from soma where synaptic input was presented (distance from soma 40–200 μm). This difference between deep and superficial excitatory cells helps compensate for the more extended morphology of deep neurons by making them electrotonically more compact. It agrees with studies showing that Ih counteracts the distance-dependent capacitive filtering of synaptic input as it propagates from dendrite to soma (Dembrow et al., 2015; Kalmbach et al., 2018b; Magee, 1999; Rall, 1967; Stuart and Spruston, 1998). Also, the differences in EPSP integration between the two excitatory subclasses are supported by the simulations without claiming that one of the subclasses has zero dendritic Ih (see, for example, Kalmbach et al., 2018b); both subclasses clearly have Ih in their apical dendrite and express HCN1 (Figure 5A). This graded effect is typically difficult to establish and shows up in our work because of the availability of large numbers of high-quality models. We conclude that the Ih conductance differences observed along the dendrites of all-active models affect their EPSP integration properties in a subclass-specific manner, an observation also supported by experiments in cortical neurons.

All-active models versus other biophysical model representations

All-active models offer enhanced biophysical realism in the form of dendritic and axonal ion channels as well as spikes initiated at the AIS for excitatory cells while also accurately capturing experimental E-features in the presence of reconstructed morphologies (Figure 6A). However, it is unclear how distinct the all-active models are with respect to other biophysical representations. We compared the all-active models with a class of models limiting the presence of ion channels to the soma region (e.g., perisomatic models; Gouwens et al., 2018; see also STAR Methods) that, for example, fail to generate spikes at the AIS (Figures 6B and 6C). When comparing all-active to perisomatic models originating from the same experiments (thus, representing the same electrophysiology and morphology data), we observed that both model types capture experimental features comparably well (Figure 6D). This, however, by no means implies similarity in the underlying model (e.g., in their conductance vectors). All-active versus perisomatic models exhibit different ion channel conductance levels along their morphology. For example, various Na^+ and K^+ conductances show differences at the soma for both spiny and aspiny cells (Figure 6E). The same applies to the AIS since perisomatic models by design

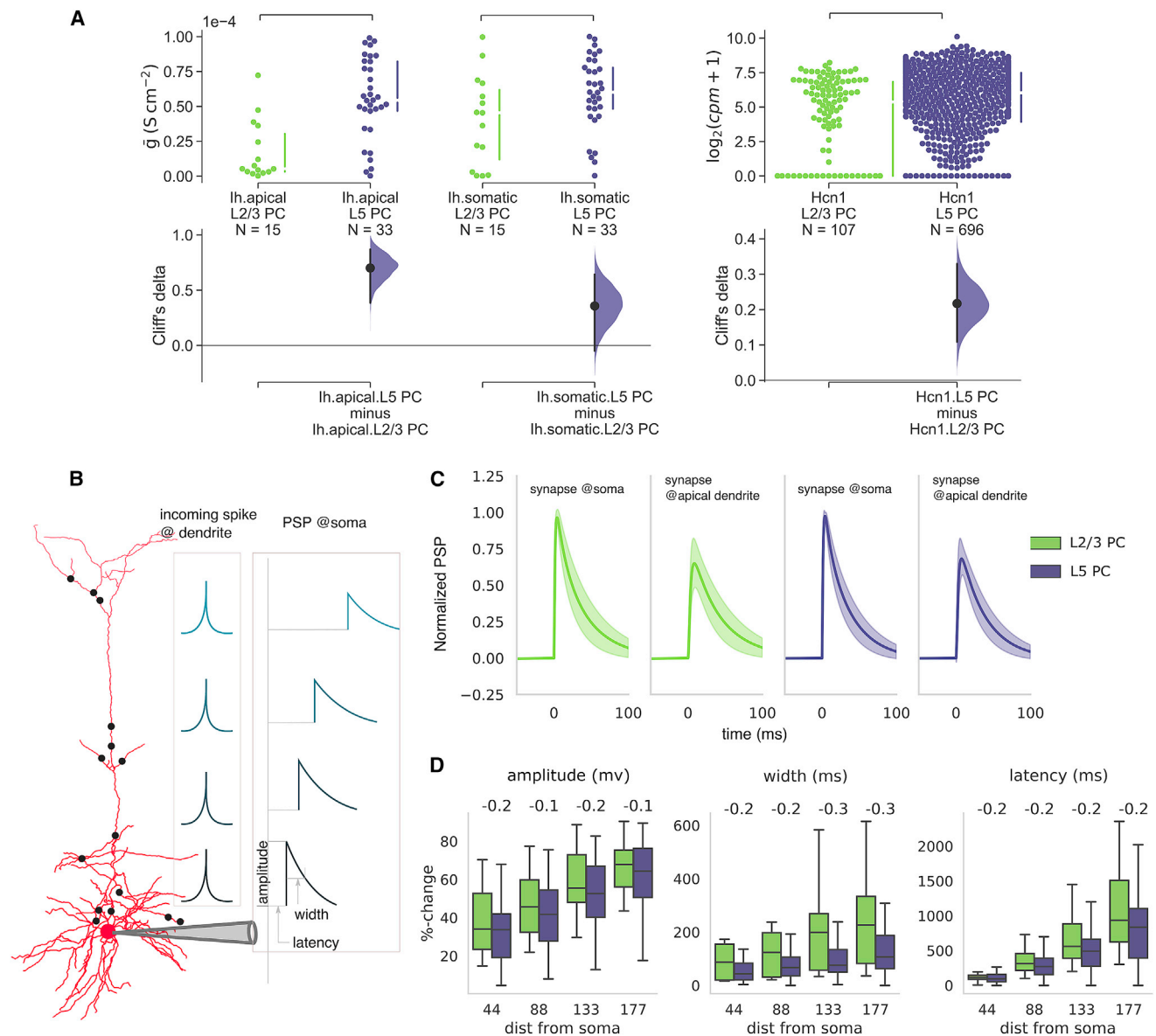


Figure 5. Increased apical Ih leads to preservation of synaptic patterns in deep versus superficial pyramidal (Pyr) neurons

(A) Left: Pairwise comparison between L2/3 and L5 excitatory models across conductances. Right: Single-cell transcriptomics comparison. (B) Simulation of synaptic activation along the apical dendrites of L2/3 and L5 Pyr neurons. Individual synapses are distributed and activated along the apical dendrite, and their postsynaptic effect is measured at the soma. Incoming presynaptic spikes along the apical dendrite (left column) and the resultant postsynaptic somatic depolarization (right column) for a single cell (CellID: 488679042). (C) Postsynaptic somatic depolarization for superficial and deep Pyr cell types normalized by the peak postsynaptic potential (PSP) amplitude when the synapse is at soma (line: mean; shaded area: standard deviation; green: L2/3 Pyr models; purple: L5 Pyr models; 15 L2/3 models; 33 L5 models; mean peak PSP amplitude of 0.75 mV and 0.56 mV for L2/3 and L5 models, respectively; synapse location: at soma and ~90 μ m from soma on the apical dendrites). (D) Comparing against the nominal case (e.g., postsynaptic event if presynaptic spike was directly injected into the soma), the percentage change in somatic postsynaptic attributes (left to right: somatic PSP response amplitude, width, and latency) as function of synapse location along the apical dendrite (line, mean; error bar, standard deviation).

do not account for active conductances anywhere else except the soma.

We already showed that differences in specific conductances in all-active models can explain divergent E-features between excitatory and inhibitory subclasses (Figures 3 and 4) and affect

synaptic integration (Figure 5). What about differences in conductances between models trained on the same experimental data? We used the Sobol-based sensitivity analysis to disentangle the role of individual conductances on E-features and observed that different conductance vectors between all-active

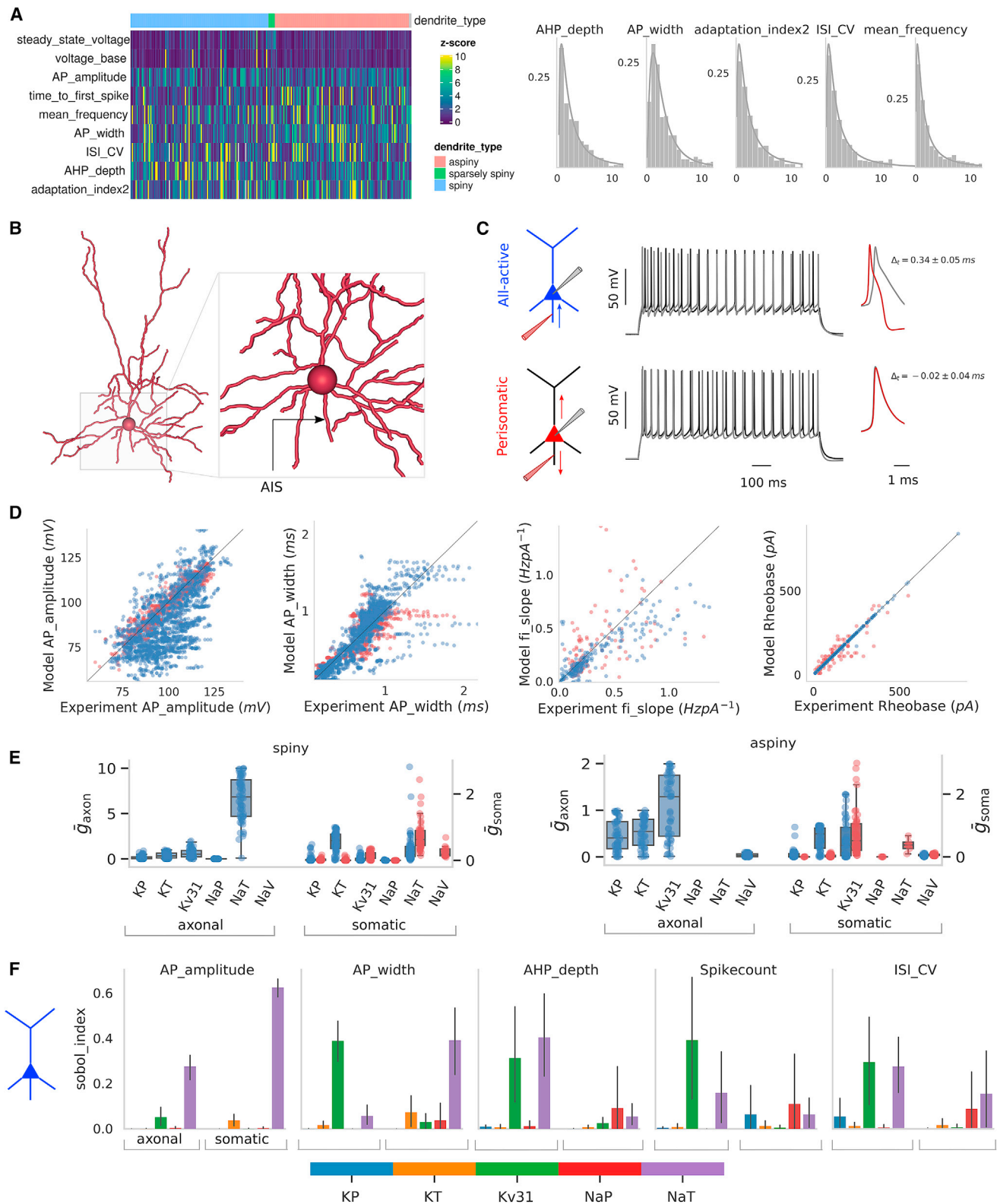


Figure 6. All-active models offer increased bio-realism

(A) Performance of 112 spiny, 109 aspiny, and 5 sparsely spiny all-active models. Left: E-features for the best models ranked according to performance (Z score) during training. Right: The histogram of the training error (Z score) for each E-feature and the associated lognormal fit.

(legend continued on next page)

and perisomatic models result in differential contributions of individual conductances to several E-features (Figures 6F and S7). Model predictions on how axonal and somatic conductances affect spike shape and excitability are drastically different between them. For all-active models, the AP width is equally affected by the axonal Kv3.1 and somatic transient Na⁺ conductance, while perisomatic models predict that somatic Kv3.1 plays the dominant role. Kv channels are important determinants of axonal membrane excitability contributing to spike initiation, shape, and temporal patterning (Rudy and McBain, 2001). Experimental studies show how Kv3 conductances can strongly impair spike repolarization and high-frequency firing in cortical subclasses. The unique properties of Kv3 channels enable sustained high-frequency firing by facilitating the recovery of transient Na channel inactivation and by minimizing the duration of the afterhyperpolarization in neocortical neurons. While not as visible on the initial firing rate, it strongly reduces firing frequency later during depolarizing steps (Erisir et al., 1999; Atzori et al., 2001). The effect of Kv3 has been predominantly reported in fast spiking GABAergic neurons (Rowan et al., 2014), with different subclasses exhibiting differential Kv3 expression (Chow et al., 1999). While experimental studies show that Kv3 is also expressed in cortical Pyr neurons (Akemann et al., 2004), the role of these conductances in non-fast spiking cells is enigmatic. The sensitivity analysis in all-active models (Figures 6E and 6F) raises an interesting possibility: While transient K, persistent K, and Kv3.1 conductances are present in comparable levels along the AIS and somata, Kv3.1 along the AIS is particularly important for shaping E-features such as the AHP depth and interspike interval (ISI) variability of spiny cells (Pedroarena, 2011). In general, we observe that the five E-features are affected by a combination of axonal and somatic conductances, whereas the perisomatic models, per design, only account for somatic contributions (often by different conductances). We conclude that while different types of biophysical models may perform comparably well on trained features, their ability to recapitulate key aspects of experimental electrophysiology, generalize and, in such manner, give rise to emergent properties, significantly depends on model setup and abstraction level.

DISCUSSION

We present a computational optimization workflow for the *en masse* generation and evaluation of bio-realistic and morphologically accurate single-cell models with active conductances along their morphology (all-active) for 230 *in vitro* experiments

from the mouse visual cortex. We use this workflow to generate 9,200 single-cell models across experiments and select either the best model or a population of best models (HOF) to represent measurements from single cells. The number of models allowed us to integrate across cell-type taxonomies and establish causal links in a multimodal dataset that consists of morphology, electrophysiology, and transcriptomics.

To assess the all-active models, we used two approaches. First, we looked at the best model compared to a specific single-cell experiment and, second, we looked into the 40 HOF models. While the best model represents a solution with the smallest training error, the 39 other HOF models generalize equally well. This points to a single experiment reflected in a family of models of similar performance rather than the existence of a single, optimal one. We also saw that the conductance vectors exhibit significantly smaller dispersion within an experiment than across major cell classes. It follows that a distinct conductance vector representation emerged among models representative of each major cell class. We then asked whether the all-active models also capture more refined excitatory and inhibitory subclasses and found that, indeed, the conductance vectors separated between distinct subclasses and, importantly, did so the same way as experimental data (E-features and transcriptomics).

Models can link seemingly disparate observations since all parameters are accessible to the experimentalist. By generating a large population of all-active models, we show that differences between models solely trained on E-features predict differentially expressed genes related to specific conductances. These results are experimentally validated by transcriptomics. Specifically, between three major inhibitory subclasses, Pvalb, Sst, and Vip, all-active models predicted differences in Kv3.1 ($\bar{g}_{Pvalb} > \bar{g}_{Sst} > \bar{g}_{Vip}$) supported by transcriptomics. Separately, we saw that E-features related to Kv3.1 also separate the three inhibitory classes, offering a causal relationship between the differences observed in the genotype (i.e., genes related to Kv3.1) and phenotype (i.e., cell classes separated by sets of E-features). All-active models of excitatory classes capture the difference in sag response also observed experimentally between L4 IT and L5 PT cells. Pairwise comparison between models of the two subclasses predicted a difference in Ih conductance, an observation that was validated when we looked at the expression of the HCN1 gene. We used the same approach in another comparison, between L5 IT and PT cells, two distinct subclasses in terms of cellular properties and conductance vectors. Again, pairwise comparisons between models of each subclass predicted differences in Ih but also in the axonal Na conductance. We found a difference in sag

(B) Reconstructed neuron morphology (CellID: 483101699).

(C) Both all-active (blue) and perisomatic (red) models capture the experimental (black) somatic voltage response, but for all-active models, spikes are initiated from the AIS; in perisomatic models, spikes start at the soma. Arrows denote the propagation direction of the spike. Right: Simulated recordings at AIS and soma depict the direction of spike propagation. $\Delta_t = t_{soma}^i - t_{axon}^i$, for the *i*th spike, is positive for all-active models and negative for perisomatic.

(D) Performance of all models on E-features (x axis: experimentally measured feature; y axis: model-produced feature after training). Each point corresponds to the feature from a single stimulus protocol. Data along the diagonal of each panel reflect 1-to-1 agreement with experimental values.

(E) Parameter combinations for all-active models for spiny (left) and aspiny (right) are different from their perisomatic counterpart (bar, mean; error bar, standard deviation).

(F) The relative contribution of AIS and somatic ion channel conductances for each intracellular somatic feature derived from the sensitivity analysis (parameter perturbation: 10% about optimized value; relative contribution of each conductance expressed in terms of Sobol indices). Results shown for all-active models of 10 excitatory cells (bar: mean; error bar: standard deviation).

response between L5 IT and PT cells linked to Ih, with several differences in experimental AP features in line with differences in axonal Na as predicted by the models. We conclude that the all-active models can unravel causal links between multimodal data not just on modalities they trained on but, importantly, also on modalities they did not train on that emerged from the optimization procedure.

An algorithm emerged to select candidate genes and ion channels responsible for the E-feature differences between two cell subclasses. It consists of the following seven steps: (1) generate models for each subclass based on E-features and reconstructed morphologies; (2) compare across the entire conductance vector between models of different cell classes; (3) assess the statistical significance of each conductance difference; (4) look for statistically significant conductance differences between subclasses; (5) look at differential expression (here, single-cell RNA-seq) for supporting evidence to determine whether difference in a conductance is related to differential expression in a related gene; (6) perform sensitivity analysis using the all-active models of the specific cell type to look for E-features that the conductance mostly affects, for the same conductance; (7) look at experiments and models for mutually supporting trends for the E-features the specific conductance mostly affects.

We use the all-active models to uncover relationships of disparate data modalities between and across cell classes. An equally important aim for models is to integrate different types of experiments of the same data modality (e.g., integrate between somatic and dendritic electrophysiology experiments) to attempt and produce the most accurate model of that particular cell class (or even specific cell/experiment; see, for example, Hay et al., 2011; Shai et al., 2015). The all-active models also offer a good starting point for such studies. For example, one can specify an additional stage of optimizations focusing on a particular ion conductance of interest in a single or a subset of existing all-active models (e.g., using dendritic experiments to constrain dendritic E-features). This process will yield models that integrate multiple data modalities and experimental observations at the soma and the dendrite of interest. Using the all-active models, such refinement will not start from scratch but may be added “on top” of existing models. This greatly reduces the complication and computational cost of such optimizations (e.g., optimizing 3–4 dendritic parameters of particular interest rather than re-running an optimization for ≥ 60 parameters). This can be done *en masse* using the hundreds of models we created for every cell subclass.

Limitations of the study

We used all-active models to determine conductance differences in a statistical manner. The outcome will be affected by salient versus more subtle differences in terms of E-features: Major ion channel expression differences between subclasses will be reflected in terms of E-features and carry over to the models and conductance vectors. However, the larger the difference in a specific conductance between two subclasses, the better the chance this difference will show in the pairwise comparison. Also, the more a specific conductance affects a single, specified E-feature, the more prominently it will be accounted for by the optimization (since models

are trained and validated on E-features and morphology). Conductances that remain “silent” during our experiments are going to be tougher to capture. In addition, the choice of sensitivity analysis is crucial to assess the impact of individual conductances on E-features. While such methods are well established for linear systems, their application becomes problematic for nonlinear processes and interactions as occurring in biophysically realistic, conductance-based models. The development of such tools is an important but underappreciated part of computational neuroscience.

A strength of all-active models is the presence of active conductances along the morphology, yet most E-features are measured in one location, the soma. In the absence of dendritic recordings, model parametrization in these distal sections is under-constrained (Larkum et al., 2009; Shai et al., 2015; Stuart and Spruston, 1998; Stuart et al., 1999). When dendritic recordings become available at scale, they will offer a useful dataset for setting up and constraining all-active models using an optimization framework very similar to the current one.

Conclusions

We present a computational optimization workflow for the *en masse* generation and evaluation of bio-realistic and morphologically accurate single-cell models with active conductances along their entire morphology. We show that all-active models preserve subclass relationships despite biological and experimental variability and offer two lines of support: the preservation of decision boundaries between broad subclasses for experiments and models (including HOF models), and the classification of subclasses based on conductance vectors. The generation of families of models representative of major cortical classes allows us to ask how these distinct classes differentiate across data modalities. Beyond a significant advancement in high-performance computing related to single-cell biophysics, the ability to search for causal relationships within and between cell types across data modalities offers a deeper understanding of the definition and functional implication of cell types in the brain.

STAR★METHODS

Detailed methods are provided in the online version of this paper and include the following:

- KEY RESOURCES TABLE
- RESOURCE AVAILABILITY
 - Lead contact
 - Materials availability
 - Data and code availability
- EXPERIMENTAL MODEL AND SUBJECT DETAILS
- METHOD DETAILS
 - Slice electrophysiology and morphology reconstructions
 - Single cell RNA sequencing and expression analysis
 - Single cell model generation and analysis
 - Postsynaptic potential (PSP) simulation with synapses
 - Classification and dimensionality reduction
- QUANTIFICATION AND STATISTICAL ANALYSIS

SUPPLEMENTAL INFORMATION

Supplemental information can be found online at <https://doi.org/10.1016/j.celrep.2022.111176>.

ACKNOWLEDGMENTS

We thank the Allen Institute founder, Paul G. Allen, for his vision, encouragement, and support. C.A.A. thanks the Board of Governors of Cedars-Sinai Medical Center. C.A.A. and S.Y.L. acknowledge the NIH grant RO1 NS120300-01. We thank Brandon Blanchard for visualizations, Fahimeh Bafizadeh for discussions, and the National Energy Research Scientific Computing Center, operated under contract no. DE-AC02-05CH11231, and the Swiss National Supercomputing Center (CSCS) for the computing resources.

AUTHOR CONTRIBUTIONS

A.N. and C.A.A. conceptualized this work. A.N., T.C., W.V.G., A.B., and C.A.A. wrote the software to develop the all-active models. A.N., T.C., Z.Y., and C.A.A. performed the formal data analysis and developed the figures. A.N., T.C., B.T., and C.A.A. wrote the manuscript with input from all of the other authors.

Received: April 13, 2020
Revised: January 28, 2022
Accepted: July 18, 2022
Published: August 9, 2022

REFERENCES

Akemann, W., Zhong, Y.-M., Ichinohe, N., Rockland, K.S., and Knöpfel, T. (2004). Transgenic mice expressing a fluorescent in vivo label in a distinct subpopulation of neocortical layer 5 pyramidal cells. *J. Comp. Neurol.* *480*, 72–88. <https://doi.org/10.1002/cne.20338>.

Anastasiades, P.G., Marlin, J.J., and Carter, A.G. (2018). Cell-type specificity of callosally evoked excitation and feedforward inhibition in the prefrontal cortex. *Cell Rep.* *22*, 679–692. <https://doi.org/10.1016/j.celrep.2017.12.073>.

Ascoli, G.A., Krichmar, J.L., Nasuto, S.J., and Senft, S.L. (2001). Generation, description and storage of dendritic morphology data. *Philos. Trans. R. Soc. Lond. B Biol. Sci.* *356*, 1131–1145.

Atzori, M., Lei, S., Evans, D.I., Kanold, P.O., Phillips-Tansey, E., McIntyre, O., and McBain, C.J. (2001). Differential synaptic processing separates stationary from transient inputs to the auditory cortex. *Nat. Neurosci.* *4*, 1230–1237. <https://doi.org/10.1038/nn760>.

Bahl, A., Stemmler, M.B., Herz, A.V.M., and Roth, A. (2012). Automated optimization of a reduced layer 5 pyramidal cell model based on experimental data. *J. Neurosci. Methods* *210*, 22–34.

Brown, S.P., and Hestrin, S. (2009). Intracortical circuits of pyramidal neurons reflect their long-range axonal targets. *Nature* *457*, 1133–1136. <https://doi.org/10.1038/nature07658>.

Chow, A., Erisir, A., Farb, C., Nadal, M.S., Ozaita, A., Lau, D., Welker, E., and Rudy, B. (1999). K⁺ channel expression distinguishes subpopulations of parvalbumin- and somatostatin-containing neocortical interneurons. *J. Neurosci.* *19*, 9332–9345.

Daigle, T.L., Madisen, L., Hage, T.A., Valley, M.T., Knoblich, U., Larsen, R.S., Takeno, M.M., Huang, L., Gu, H., Larsen, R., et al. (2018). A suite of transgenic driver and reporter mouse lines with enhanced brain-cell-type targeting and functionality. *Cell* *174*, 465–480.e22. <https://doi.org/10.1016/j.cell.2018.06.035>.

Hines, M., Davison, A.P., and Muller, E. (2009). NEURON and Python. *Front. Neuroinform.* *3*, 1.

Dembrow, N.C., Chitwood, R.A., and Johnston, D. (2010). Projection-specific neuromodulation of medial prefrontal cortex neurons. *J. Neurosci.* *30*, 16922–16937. <https://doi.org/10.1523/JNEUROSCI.3644-10.2010>.

Dembrow, N.C., Zemelman, B.V., and Johnston, D. (2015). Temporal dynamics of L5 dendrites in medial prefrontal cortex regulate integration versus coincidence detection of afferent inputs. *J. Neurosci.* *35*, 4501–4514. <https://doi.org/10.1523/JNEUROSCI.4673-14.2015>.

Druckmann, S., Banitt, Y., Gidon, A., Schürmann, F., Markram, H., and Segev, I. (2007). A novel multiple objective optimization framework for constraining conductance-based neuron models by experimental data. *Front. Neurosci.* *1*, 7–18.

Druckmann, S., Berger, T.K., Schürmann, F., Hill, S., Markram, H., and Segev, I. (2011). Effective stimuli for constructing reliable neuron models. *PLoS Comput. Biol.* *7*, e1002133.

Erisir, A., Lau, D., Rudy, B., and Leonard, C.S. (1999). Function of specific K⁺ channels in sustained high-frequency firing of fast-spiking neocortical interneurons. *J. Neurophysiol.* *82*, 2476–2489.

Eyal, G., Verhoog, M.B., Testa-Silva, G., Deitcher, Y., Benavides-Piccione, R., DeFelipe, J., De Kock, C.P.J., Mansvelde, H.D., and Segev, I. (2018). Human cortical pyramidal neurons: from spines to spikes via models. *Front. Cell. Neurosci.* *12*, 181.

Fortin, F.-A., De Rainville, F.-M., Gardner, M.-A., Parizeau, M., and Gagné, C. (2012). {DEAP}: evolutionary algorithms made easy. *J. Mach. Learn. Res.* *13*, 2171–2175.

Goldin, A.L., Barchi, R.L., Caldwell, J.H., Hofmann, F., Howe, J.R., Hunter, J.C., Kallen, R.G., Mandel, G., Meisler, M.H., Netter, Y.B., et al. (2000). Nomenclature of voltage-gated sodium channels. *Neuron* *28*, 365–368. [https://doi.org/10.1016/S0896-6273\(00\)00116-1](https://doi.org/10.1016/S0896-6273(00)00116-1).

Gouwens, N.W., Berg, J., Feng, D., Sorensen, S.A., Zeng, H., Hawrylycz, M.J., Koch, C., and Arkhipov, A. (2018). Systematic generation of biophysically detailed models for diverse cortical neuron types. *Nat. Commun.* *9*, 710.

Gouwens, N.W., Sorensen, S.A., Berg, J., Lee, C., Jarsky, T., Ting, J., Sunkin, S.M., Feng, D., Anastassiou, C.A., Barkan, E., et al. (2019). Classification of electrophysiological and morphological neuron types in the mouse visual cortex. *Nat. Neurosci.* *22*, 1182–1195.

Tennøe, S., Halmes, G., and Einevoll, G.T. (2018). Uncertainpy: a Python toolbox for uncertainty quantification and sensitivity analysis in computational neuroscience. *Front. Neuroinform.* *12*, 49.

Hattox, A.M., and Nelson, S.B. (2007). Layer V neurons in mouse cortex projecting to different targets have distinct physiological properties. *J. Neurophysiol.* *98*, 3330–3340. <https://doi.org/10.1152/jn.00397.2007>.

Hay, E., Hill, S., Schürmann, F., Markram, H., and Segev, I. (2011). Models of neocortical layer 5b pyramidal cells capturing a wide range of dendritic and perisomatic active properties. *PLoS Comput. Biol.* *7*, e1002107.

Hille, B. (1978). Ionic channels in excitable membranes. Current problems and biophysical approaches. *Biophys. J.* *22*, 283–294.

Hines, M.L., and Carnevale, N.T. (1997). The NEURON simulation environment. *Neural Comput.* *9*, 1179–1209.

Ho, J., Tumkaya, T., Aryal, S., Choi, H., and Claridge-Chang, A. (2019). Moving beyond P values: data analysis with estimation graphics. *Nat. Methods* *16*, 565–566.

Hodge, R.D., Bakken, T.E., Miller, J.A., Smith, K.A., Barkan, E.R., Graybiel, L.T., Close, J.L., Long, B., Johansen, N., Penn, O., et al. (2019). Conserved cell types with divergent features in human versus mouse cortex. *Nature* *573*, 61–68.

Hogan, Q.H., and Poroli, M. (2008). Hyperpolarization-activated current (I_h) contributes to excitability of primary sensory neurons in rats. *Brain Res.* *1207*, 102–110.

Kalmbach, B.E., Buchin, A., Long, B., Close, J., Nandi, A., Miller, J.A., Bakken, T.E., Hodge, R.D., Chong, P., de Frates, R., et al. (2018a). H-channels contribute to divergent intrinsic membrane properties of supragranular pyramidal neurons in human versus mouse cerebral cortex. *Neuron* *100*, 1194–1208.e5.

Kalmbach, B.E., Buchin, A., Long, B., Close, J., Nandi, A., Miller, J.A., Bakken, T.E., Hodge, R.D., Chong, P., de Frates, R., et al. (2018b). H-channels contribute to divergent intrinsic membrane properties of supragranular

- pyramidal neurons in human versus mouse cerebral cortex. *Neuron* 100, 1194–1208.e5. <https://doi.org/10.1016/j.neuron.2018.10.012>.
- Katz, E., Stoler, O., Scheller, A., Khrapunsky, Y., Goebbels, S., Kirchhoff, F., Gutnick, M.J., Wolf, F., and Fleidervish, I.A. (2018). Role of sodium channel subtype in action potential generation by neocortical pyramidal neurons. *Proc. Natl. Acad. Sci. USA* 115, E7184–E7192. <https://doi.org/10.1073/pnas.1720493115>.
- Kawaguchi, Y. (2017). Pyramidal cell subtypes and their synaptic connections in layer 5 of rat frontal cortex. *Cereb. Cortex* 27, 5755–5771. <https://doi.org/10.1093/cercor/bhx252>.
- Kim, E.J., Juvinett, A.L., Kyubwa, E.M., Jacobs, M.W., and Callaway, E.M. (2015). Three types of cortical layer 5 neurons that differ in brain-wide connectivity and function. *Neuron* 88, 1253–1267. <https://doi.org/10.1016/j.neuron.2015.11.002>.
- Lai, H.C., and Jan, L.Y. (2006). The distribution and targeting of neuronal voltage-gated ion channels. *Nat. Rev. Neurosci.* 7, 548–562.
- Larkum, M.E., Nevian, T., Sandler, M., Polsky, A., and Schiller, J. (2009). Synaptic integration in tuft dendrites of layer 5 pyramidal neurons: a new unifying principle. *Science* 325, 756–760. <https://doi.org/10.1126/science.1171958>.
- Lien, C.-C., and Jonas, P. (2003). Kv3 potassium conductance is necessary and kinetically optimized for high-frequency action potential generation in hippocampal interneurons. *J. Neurosci.* 23, 2058–2068.
- Magee, J.C. (1999). Erratum: dendritic I_h normalizes temporal summation in hippocampal CA1 neurons. *Nat. Neurosci.* 2, 848. <https://doi.org/10.1038/12229>.
- Mainen, Z.F., Joerges, J., Huguenard, J.R., and Sejnowski, T.J. (1995). A model of spike initiation in neocortical pyramidal neurons. *Neuron* 15, 1427–1439.
- Gupta, A., Wang, Y., and Markram, H. (2000). Organizing principles for a diversity of GABAergic interneurons and synapses in the neocortex. *Science* 287, 273–278. <https://doi.org/10.1126/science.287.5451.273>.
- Markram, H., Toledo-Rodriguez, M., Wang, Y., Gupta, A., Silberberg, G., and Wu, C. (2004). Interneurons of the neocortical inhibitory system. *Nat. Rev. Neurosci.* 5, 793–807. <https://doi.org/10.1038/nrn1519>.
- McMahon, A., Fowler, S.C., Perney, T.M., Akemann, W., Knöpfel, T., and Joho, R.H. (2004). Allele-dependent changes of olivocerebellar circuit properties in the absence of the voltage-gated potassium channels Kv3. 1 and Kv3. 3. *Eur. J. Neurosci.* 19, 3317–3327.
- Mehaffey, W.H., Maler, L., and Turner, R.W. (2008). Intrinsic frequency tuning in ELL pyramidal cells varies across electrosensory maps. *J. Neurophysiol.* 99, 2641–2655.
- Miettinen, K. (2012). *Nonlinear Multiobjective Optimization* (Springer Science & Business Media).
- Mosher, C.P., Wei, Y., Kamiński, J., Nandi, A., Mamelak, A.N., Anastassiou, C.A., and Rutishauser, U. (2020). Cellular classes in the human brain revealed in vivo by heartbeat-related modulation of the extracellular action potential waveform. *Cell Rep.* 30, 3536–3551.e6. <https://doi.org/10.1016/j.celrep.2020.02.027>.
- Muona, M., Berkovic, S.F., Dibbens, L.M., Oliver, K.L., Maljevic, S., Bayly, M.A., Joensuu, T., Canafoglia, L., Franceschetti, S., Michelucci, R., et al. (2015). A recurrent de novo mutation in KCNC1 causes progressive myoclonus epilepsy. *Nat. Genet.* 47, 39–46.
- Noujaim, S.F., Kaur, K., Milstein, M., Jones, J.M., Furspan, P., Jiang, D., Auerbach, D.S., Herron, T., Meisler, M.H., and Jalife, J. (2012). A null mutation of the neuronal sodium channel Nav1.6 disrupts action potential propagation and excitation-contraction coupling in the mouse heart. *Faseb. J.* 26, 63–72. <https://doi.org/10.1096/fj.10-179770>.
- Palacios, J., Iidakanari, Zisis, E., Mike, G., Vanherpe, L., Courcol, J.-D., and Amsalem, O. (2016). BlueBrain/NeuroM: v1.2.0. <https://doi.org/10.5281/zenodo.209498>.
- Pedregosa, F., Varoquaux, G., Gramfort, A., Michel, V., Thirion, B., Grisel, O., Blondel, M., Prettenhofer, P., Weiss, R., Dubourg, V., et al. (2011). Scikit-learn: machine learning in Python. *J. Mach. Learn. Res.* 12, 2825–2830.
- Pedroarena, C.M. (2011). BK and Kv3. 1 potassium channels control different aspects of deep cerebellar nuclear neurons action potentials and spiking activity. *Cerebellum* 10, 647–658.
- Peng, H., Bria, A., Zhou, Z., Iannello, G., and Long, F. (2014). Extensible visualization and analysis for multidimensional images using Vaa3D. *Nat. Protoc.* 9, 193–208.
- Porcello, D.M., Ho, C.S., Joho, R.H., and Huguenard, J.R. (2002). Resilient RTN fast spiking in Kv3. 1 null mice suggests redundancy in the action potential repolarization mechanism. *J. Neurophysiol.* 87, 1303–1310.
- Poulin, J.-F., Tasic, B., Hjerling-Leffler, J., Trimarchi, J.M., and Awatramani, R. (2016). Disentangling neural cell diversity using single-cell transcriptomics. *Nat. Neurosci.* 19, 1131–1141.
- Prinz, A.A., Billimoria, C.P., and Marder, E. (2003). Alternative to hand-tuning conductance-based models: construction and analysis of databases of model neurons. *J. Neurophysiol.* 90, 3998–4015.
- Rall, W. (1967). Distinguishing theoretical synaptic potentials computed for different soma-dendritic distributions of synaptic input. *J. Neurophysiol.* 30, 1138–1168. <https://doi.org/10.1152/jn.1967.30.5.1138>.
- Raman, I.M., Sprunger, L.K., Meisler, M.H., and Bean, B.P. (1997). Altered subthreshold sodium currents and disrupted firing patterns in purkinje neurons of Scn8a mutant mice. *Neuron* 19, 881–891. [https://doi.org/10.1016/S0896-6273\(00\)80969-1](https://doi.org/10.1016/S0896-6273(00)80969-1).
- Rowan, M.J.M., Tranquil, E., and Christie, J.M. (2014). Distinct Kv channel subtypes contribute to differences in spike signaling properties in the axon initial segment and presynaptic boutons of cerebellar interneurons. *J. Neurosci.* 34, 6611–6623.
- Royeck, M., Horstmann, M.-T., Remy, S., Reitze, M., Yaari, Y., and Beck, H. (2008). Role of axonal Nav1.6 sodium channels in action potential initiation of CA1 pyramidal neurons. *J. Neurophysiol.* 100, 2361–2380. <https://doi.org/10.1152/jn.90332.2008>.
- Rudy, B., and McBain, C.J. (2001). Kv3 channels: voltage-gated K⁺ channels designed for high-frequency repetitive firing. *Trends Neurosci.* 24, 517–526.
- Rumbell, T.H., Draguljčić, D., Yadav, A., Hof, P.R., Luebke, J.I., and Weaver, C.M. (2016). Automated evolutionary optimization of ion channel conductances and kinetics in models of young and aged rhesus monkey pyramidal neurons. *J. Comput. Neurosci.* 41, 65–90.
- Shai, A.S., Anastassiou, C.A., Larkum, M.E., and Koch, C. (2015). Physiology of layer 5 pyramidal neurons in mouse primary visual cortex: coincidence detection through bursting. *PLoS Comput. Biol.* 11, e1004090. <https://doi.org/10.1371/journal.pcbi.1004090>.
- Sittl, R., Carr, R.W., and Grafe, P. (2011). Sustained increase in the excitability of myelinated peripheral axons to depolarizing current is mediated by Nav1.6. *Neurosci. Lett.* 492, 129–133. <https://doi.org/10.1016/j.neulet.2011.01.069>.
- Sorensen, S.A., Bernard, A., Menon, V., Royall, J.J., Glattfelder, K.J., Desta, T., Hirokawa, K., Mortrud, M., Miller, J.A., Zeng, H., et al. (2015). Correlated gene expression and target specificity demonstrate excitatory projection. *Cereb. Cortex* 25, 433–449. <https://doi.org/10.1093/cercor/bht243>.
- Stuart, G., and Spruston, N. (1998). Determinants of voltage attenuation in neocortical pyramidal neuron dendrites. *J. Neurosci.* 18, 3501–3510. <https://doi.org/10.1523/JNEUROSCI.18-10-03501.1998>.
- Stuart, G., Spruston, N., and Häusser, M. (1999). *Dendrites* (Oxford University Press).
- Tang, F., Barbacioru, C., Wang, Y., Nordman, E., Lee, C., Xu, N., Wang, X., Bodeau, J., Tuch, B.B., Siddiqui, A., et al. (2009). mRNA-Seq whole-transcriptome analysis of a single cell. *Nat. Methods* 6, 377–382.
- Tasic, B., Menon, V., Nguyen, T.N., Kim, T.K., Jarsky, T., Yao, Z., Levi, B., Gray, L.T., Sorensen, S.A., Dolbeare, T., et al. (2016). Adult mouse cortical cell taxonomy revealed by single cell transcriptomics. *Nat. Neurosci.* 19, 335–346.
- Tasic, B., Yao, Z., Graybuck, L.T., Smith, K.A., Nguyen, T.N., Bertagnolli, D., Goldy, J., Garren, E., Economo, M.N., Viswanathan, S., et al. (2018a). Shared and distinct transcriptomic cell types across neocortical areas. *Nature* 563, 72–78.

Tasic, B., Yao, Z., Graybiel, L.T., Smith, K.A., Nguyen, T.N., Bertagnolli, D., Goldy, J., Garren, E., Economo, M.N., Viswanathan, S., et al. (2018b). Shared and distinct transcriptomic cell types across neocortical areas. *Nature* **563**, 72–78. <https://doi.org/10.1038/s41586-018-0654-5>.

Teeter, C., Iyer, R., Menon, V., Gouwens, N., Feng, D., Berg, J., Szafer, A., Cain, N., Zeng, H., Hawrylycz, M., et al. (2018). Generalized leaky integrate-and-fire models classify multiple neuron types. *Nat. Commun.* **9**, 709.

Teeters, J.L., Godfrey, K., Young, R., Dang, C., Friedsam, C., Wark, B., Asari, H., Peron, S., Li, N., Peyrache, A., et al. (2015). Neurodata without borders: creating a common data format for neurophysiology. *Neuron* **88**, 629–634.

Tibshirani, R., Walther, G., and Hastie, T. (2001). Estimating the number of clusters in a data set via the gap statistic. *J. Roy. Stat. Soc. B* **63**, 411–423.

Tremblay, R., Lee, S., and Rudy, B. (2016). GABAergic interneurons in the neocortex: from cellular properties to circuits. *Neuron* **91**, 260–292. <https://doi.org/10.1016/j.neuron.2016.06.033>.

Van Geit, W., Gevaert, M., Chindemi, G., Rössert, C., Courcol, J.-D., Muller, E.B., Schürmann, F., Segev, I., and Markram, H. (2016). BluePyOpt: leveraging open source software and cloud infrastructure to optimise model parameters in neuroscience. *Front. Neuroinform.* **10**, 17.

Wymore, R.S., Korenberg, J.R., Kinoshita, K.D., Aiyar, J., Coyne, C., Chen, X.-N., Hustad, C.M., Copeland, N.G., Gutman, G.A., Jenkins, N.A., et al. (1994). Genomic organization, nucleotide sequence, biophysical properties, and localization of the voltage-gated K⁺ channel gene *KCNA4/Kv1.4* to mouse chromosome 2/human 11p14 and mapping of *KCNC1/Kv3.1* to mouse 7/human 11p14. 3-p15. 2 and *KCNA1/Kv1.1* to human. *Genomics* **20**, 191–202.

Zeisel, A., Muñoz-Manchado, A.B., Codeluppi, S., Lönnerberg, P., La Manno, G., Juréus, A., Marques, S., Munguba, H., He, L., Betsholtz, C., et al. (2015). Cell types in the mouse cortex and hippocampus revealed by single-cell RNA-seq. *Science* **347**, 1138–1142.

STAR★METHODS

KEY RESOURCES TABLE

REAGENT or RESOURCE	SOURCE	IDENTIFIER
Deposited data		
Single-cell Transcriptomic Data	Allen Institute for Brain Science	https://portal.brain-map.org/atlasses-and-data/maseq
Single-Cell Electrophysiology and Morphology	Allen Institute for Brain Science	https://celltypes.brain-map.org/
Single-neuron biophysical perisomatic models	Allen Institute for Brain Science	https://portal.brain-map.org/explore/models/perisomatic-single-neurons
Software and algorithms		
Python	Python.org	RRID: SCR_008394
Neuron 7.5 Simulator	NEURON	RRID: SCR_005393
scikit-learn: machine learning in Python	http://scikit-learn.org	RRID:SCR_002577
Brain Modeling Toolkit	Allen Institute for Brain Science	https://github.com/AllenInstitute/bmtk
Allen Institute Software Development Kit	Allen Institute for Brain Science	http://github.com/AllenInstitute/AllenSDK
Blue Brain Optimization Toolbox (BluePyOpt)	Blue Brain Project	https://github.com/BlueBrain/BluePyOpt
Electrophys Feature Extraction Library (eFEL)	Blue Brain Project	https://github.com/BlueBrain/eFEL
Neuron Morphology Analysis Toolkit (NeuroM)	Blue Brain Project	https://github.com/BlueBrain/NeuroM
Uncertainpy: A Python Toolbox for Uncertainty Quantification	Tennøe et al. (2018)	https://github.com/simetenn/uncertainpy
All-active Modeling Workflow	This manuscript	https://github.com/AllenInstitute/All-active-Workflow
Clustering, Classification, RNA-seq data analysis, Simulation, Visualization and All-active Models	This manuscript	https://github.com/AllenInstitute/All-active-Manuscript

RESOURCE AVAILABILITY

Lead contact

Further information and requests for resources and reagents should be directed to and will be fulfilled by the lead contact, Costas A. Anastassiou (costas.anastassiou@gmail.com, costasa@alleninstitute.org, costas.anastassiou@cshs.org).

Materials availability

The all-active single-neuron models as well as the single-cell RNAseq data used in this manuscript are publicly available for download (see [Key resources table](#)). This study did not generate new unique reagents.

Data and code availability

- This paper analyzes existing, publicly available data. The accession numbers for the datasets are listed in the [key resources table](#).
- The automated staged optimization workflow is available as a python package (All-active Workflow), with BluePyOpt being the main procedure for the evolutionary multi-objective optimization. The data analysis, visualization and the all-active models developed in this work have been deposited in a separate [repository](#). All code is publicly accessible as of the date of publication. DOIs are listed in the [key resources table](#).
- Any additional information required to reanalyze the data reported in this paper is available from the [lead contact](#) upon request.

EXPERIMENTAL MODEL AND SUBJECT DETAILS

Acute brain slices were prepared from male or female mice between the ages of P45 to P70 that expressed Ai14 and crossed with a specific Cre driver line. Mice are group-housed (5 per cage) in micro ventilated cages with a 12 h light/dark cycle. Purina Lab diet 5001 mouse food and water are given *ad libitum*. Cells from the following driver lines are used for model generation: Vipr2-IRES2-Cre, Ndnf-IRES2-dgCre, Nos1-CreERT2, Pvalb-IRES-Cre, Nkx2-1-CreERT2, Sst-IRES-Cre, Chrna2-Cre_OE25, Oxt-T2A-Cre, Htr3a-Cre_NO152, Vip-IRES-Cre, Ctgf-T2A-dgCre, Slc17a6-IRES-Cre, Slc32a1-IRES-Cre, Tlx3-Cre_PL56, Scnn1a-Tg2-Cre, Scnn1a-Tg3-Cre, Nr5a1-Cre, Esr2-IRES2-Cre, Rbp4-Cre_KL100, Ntsr1-Cre_GN220, Rorb-IRES2-Cre, Cux2-CreERT2.

METHOD DETAILS

Slice electrophysiology and morphology reconstructions

The electrophysiology and morphology data are part of the Allen Cell-Types Database (2015). Whole cell patch clamp recordings were performed on single neurons in prepared slices from adult mouse visual cortex. Fluorescence illumination was used to identify the Cre-positive neurons based on tdTomato fluorescence. Time series for the voltage response under stimuli of varied amplitude and duration for standardized set of protocols (step, ramp, colored noise) are collected in an.nwb (Teeters et al., 2015) format at 34°C and corrected for liquid junction potential (−14 mV). Following the recording protocols the neurons are filled with biocytin, present in the intracellular patch electrode. Sections are processed using 3,3'-diaminobenzidine (DAB) peroxidase substrate kit to identify recorded neurons filled with biocytin. Serial images (63× magnification) through biocytin-filled neurons are evaluated for quality, and cells that passed a quality threshold are entered in a detailed morphological analysis workflow. The dendritic morphology of each neuron is identified as either aspiny, sparsely spiny or spiny. Reconstructions are generated for a subset of neurons using a 3D Visualization-Assisted Analysis (Vaa3D) (Peng et al., 2014) workflow. Separately, the automated 3D reconstruction results are manually curated using the Mozak extension of Vaa3D and subsequently saved in the swc format. The electrophysiology and morphology procedures along with the immunohistological staining are detailed in the technical white papers of the cell-types database (2015).

Single cell RNA sequencing and expression analysis

Materials and methods used for single cell RNA collection and sequencing are described in (Tasic et al., 2016). Briefly, single cells from visual cortex of adult transgenic mice were labeled and isolated by FACS (fluorescence activated sorting). SMART-Seq Ultra Low Input RNA Kit for Illumina Sequencing was used for cDNA synthesis of single-cell RNA and subsequent amplification. Further downstream analysis involved aligning reads and QC. This data is freely available through the Allen Brain Atlas data portal (<https://portal.brain-map.org/atlas-and-data/maseq>).

The broad subclass definition used throughout this paper consists of three primary inhibitory lines, Pvalb basket cells, Sst, and Vip bipolar inhibitory cells. A fourth excitatory class 'Pyr' is composed of spiny Rorb-Ires2, Scnn1a-Tg2,3, Nr5a1 and Rbp4 cells. For classification and comparison between classes, a target subclass, broad or refined, is required to have at least 10 member cells.

We used the cell-type mappings (morpho-electric or ME type to transcriptomic refined subclass) derived in (Gouwens et al., 2019) to reconcile between the different datasets, namely RNA-seq and morpho-electric data. We performed additional filtering to ensure consistency in comparing classes across the two datasets. First, we labeled Cre-lines in the ME data not sampled in the RNA-seq data as 'Other' (Figure 1B) and did not use them in any cell class definitions. The only exception to this rule is Rorb-Ires2-Cre, a member of the Pyr class, since a significant portion of these cells were sampled during model generation. For the analysis of the inhibitory classes, we kept the comparisons limited to basket cells within the Pvalb class (by filtering out Chandelier cells, i.e. Pvalb-Vipr2 labeled cells with qualitative morphology label 'Chandelier').

Single cell model generation and analysis

The biophysical models are simulated in the NEURON 7.5 (Hines and Carnevale, 1997) simulation environment via python interface (Hines et al., 2009) with variable time step integration. Due to the inconsistencies in the axonal reconstructions, we have uniformly replaced the axons (irrespective of their presence in the swc file (Ascoli et al., 2001)) with a 60 μm stub that has a diameter of 1 μm. We did so after using `Import3d_SWC_read()` function to read the morphology file (swc format) in NEURON. For model generation we used a combination of the following active ion channels: I_h , NaT, NaP, KT, KP, Kv2, Kv3.1, SK, I_m , Ca_{LVA} , Ca_{HVA} for apical, basal dendrites, soma and AIS. At exploratory stages of the workflow design, we found that optimizing the entire parameter vector (43 variables) in a single stage led to poorer convergence. We attribute this to improper setting of the passive properties with models exhibiting particular sensitivity to these parameters. To address this point, we used separate optimization stages with the first one (Stage 0) focusing on passive parameters only, i.e. cm , Ra , g_{pas} , e_{pas} . Stage 0 thus aims at optimizing the baseline response properties of the model though the same passive parameters remain optimization targets in the subsequent optimization stages. In addition, we also observed that lumping the h-channel conductance as well as other active channels in a single optimization stage and adding the deviation between the model and experimental sag to the objective vector resulted in the suprathreshold component of the error vector dominating the resultant model generations. To address this issue, we introduced a separate optimization stage for the h-channel conductance (Stage 1) followed by a third stage that includes the rest of the active channels (Stage 2).

We used a 1s long dc current step for eliciting the neural response in experiments and models. In total, we use 15 electrophysiology features over 3 stages: resting potential before and after current injection (voltage base, steady state voltage), average membrane potential during stimulation (voltage deflection), spike frequency, ISI slope, adaptation index, time-to-first-spike, AP amplitude and width, AHP depth (<https://doi.org/10.5281/zenodo.1283474>). Models are evaluated against the experimental features with respect to z-score = $\frac{|f_i - \mu_i|}{\sigma_i}$, where the feature value f_i is measured from the output traces of the models while μ_i and σ_i are the experimentally measured mean and standard deviation, respectively, for the targeted electrophysiology features. From the definition, when z-score = 1, model and experiments are within one standard deviation of the experiment. The experimental standard deviation for each feature is calculated over repetitions of the same stimulus; in absence of repetition, we use 5% of the mean as the default standard deviation. During training we use the `force_max_score = True` option in the `efeature` module of `BluePyOpt` such that maximum

error, i.e., z-score for any objective between model and experiment is bounded by 250. A common example when this option will be triggered is when in comparison to a spiking trace in the experiment the model for the same stimulus produces a subthreshold response. The 3-stage all-active model optimization workflow looks as follows:

1. Stage 0: fit passive membrane properties of the model along the entire single-cell morphology on subthreshold, non-spiking features of an experiment for a number of stimulation amplitudes (# of training objectives = $4 \times$ # subthreshold traces; # generations = 50; # seeds = 1),
2. Stage 1: include the h-channel conductance and re-fit along the entire single-cell morphology on subthreshold experimental features (# of training objectives = $5 \times$ # subthreshold traces; # generations = 50; # seeds = 1). We selected h-channels to include in the intermediate stage to fully characterize the subthreshold responses before exposing the models to the battery of stimulus driving spiking behavior.
3. Stage 2: fit all active Na^+ , K^+ and Ca^{++} conductances on subthreshold and spiking features for a number of experimental stimulus amplitudes (# training objectives = 11×2 spiking traces + spikecount at rheobase trace and the maximal subthreshold trace; # generations = 200; # seeds = 4).

We have released this optimization workflow as a python package (<https://github.com/AllenInstitute/All-active-Workflow>) and the staged workflow can be easily configured via nested json schemas.

The list of parameters, their description as well as their bounds and the stimulus set used at each stage to inform the optimization is detailed in [Tables S1-S3](#). Using this model optimization workflow, approximately 600,000 models are tested during the development stage. It follows that this procedure is associated with a significant computational demand, i.e. the CPU demand per cell at the in-house computing cluster is 26 ± 11 hours on a 256×2.2 GHz Intel Xeon E5-2630v4 processor rack for a 2:1 offspring to core ratio. We tested and deployed the same optimization workflow in 3 other computing systems: Amazon Web Services EC2, NERSC and Blue Brain 5 Supercomputers ([Figure S9](#)). However, we were able to drastically improve the computation demand (approx. by factor 8–10) by adding a timeout functionality to the evolutionary algorithm subroutine, where models for which their evaluation surpassed the set timeout parameter are rejected with maximum score across all objectives ([Figure S10](#)).

The model generation has a final validation stage - where the models go through the entire stimulus battery of the corresponding experiment. In particular, we calculate two more metrics along with the average training error (z-score) across all the objectives, namely, Feature average Train : the Feature Average Generalization, which is the average z-score of the 15 features used in the optimization for all the 1 s long DC stimuli not part of the training set in Stage 2. Finally, we also calculated the ratio of the trial-to-trial explained variance (EV) ([Gouwens et al., 2018](#); [Teeter et al., 2018](#)) of the spike times for colored noise, a stimulus type the model has not seen at any level of the model generation. The EV is defined as

$$EV = \frac{\sigma^2(r_{\text{exp}}) + \sigma^2(r_{\text{model}}) - \sigma^2(r_{\text{exp}} - r_{\text{model}})}{\sigma^2(r_{\text{exp}}) + \sigma^2(r_{\text{model}})} \times 100$$

where σ^2 is the variance of the Peri Stimulus Histogram (PSTH) denoted by r . The experiment r_{exp} and model r_{model} are calculated by convolving the respective spike trains with a gaussian curve at a bin window of 10 ms. We report these metrics for all 40 hall of fame models across the 4 seeds.

We have also published a jupyter notebook where we include examples of how to use these all-active models and extend them to include even more complicated biophysics, e.g., backpropagating action potential (bAP). Thus, the all-active models can also be used as a good starting point or “basis models” that, in a second step, can be tailored accordingly to specific needs and mechanisms.

Postsynaptic potential (PSP) simulation with synapses

The models developed here are consistent with the Allen Institute biophysical format and thus, can be simulated in a network in presence of synapses using Brain Modeling Toolkit (bmtk). The PSP simulation results shown in [Figures 5C and 5D](#) are computed for excitatory synapses with standard parameterization. In short, we used NEURON’s Exp2Syn mechanism with the following parameters: $\tau_1 = 1$ ms, $\tau_2 = 3$ ms, $E_{\text{rev}} = 0$ mV and $g_{\text{syn}} = 1e-4$.

Classification and dimensionality reduction

In [Figures 2C and 2D](#) we used the UMAP transform (github.com/lmcinnes/umap) with $n_{\text{neighbors}} = 10$, again in a pipeline with the `scikit-learn StandardScaler()`. To enable comparisons between experiments and models for embedded electrophysiological features (at the maximal 1 s long DC step current used in training), we learn the manifold on the experimental features and use the `transform()` method in UMAP to force ‘new data’ (model ephys features) in the same 2D space. We use `scikit-learn KMeans()` for an unsupervised clustering of the reduced ephys features and consequently draw the decision boundary by assigning cluster tag by sampling uniformly from the 2D grid. The optimal no. of clusters in KMeans is determined using the gap statistic ([Tibshirani et al., 2001](#)).

We used the Random-Forest classifier (`RandomForestClassifier()`) within Scikit-learn ([Pedregosa et al., 2011](#)) library for our classification results in [Figure S8](#). To construct the different combinations of feature vectors we employed the ephys features used in training for model generation, morphological features, and, finally, the model parameter set with least training error. For

morphological feature extraction and analysis we used the python package NeuroM (Palacios et al., 2016) to extract the following features from the input .swc reconstructions: soma_surface, soma_radius, and length, area, volume, taper_rate for all the neurites (tree of sections), i.e., apical, basal dendrite, axon. For model-based feature construction we only consider parameters shared by all cells to prevent trivial differences between excitatory and inhibitory cells from dominating the outcome (e.g., no apical dendrites for aspiny/sparsely spiny cell reconstructions or differences in conductance recipe, Table S1, built into the model generation pipeline). We use a standard data augmentation technique of including 20 hof models when training the classifier for the model parameter-only feature set. The five feature sets in Figure S8C comprise of 7, 23, 25, 41 features each. F1 score is reported on a stratified test set with 70–30 train-test split of the data and averaged over 3 independent shuffles; The importance of a feature (Figure S8A) simply corresponds to average reduction in gini impurity for nodes that use that specific feature.

QUANTIFICATION AND STATISTICAL ANALYSIS

All statistical analysis were performed in python using the statsmodels (Seabold et al., 2010) and DABEST (Ho et al., 2019) packages. Mann-Whitney U-test is used extensively to compare conductance densities and gene expression across cell-types and statistical significance are indicated as *: p-val < 0.05, **: p-val < 10^{-2} , ***: p-val < 10^{-3} after adjusting for a False Discovery Rate (FDR) of 5%. The effect size between distributions were computed using the Cliff's delta statistic.

Cell Reports, Volume 40

Supplemental information

**Single-neuron models linking electrophysiology,
morphology, and transcriptomics
across cortical cell types**

Anirban Nandi, Thomas Chartrand, Werner Van Geit, Anatoly Buchin, Zizhen Yao, Soo Yeun Lee, Yina Wei, Brian Kalmbach, Brian Lee, Ed Lein, Jim Berg, Uygur Sümbül, Christof Koch, Bosiljka Tasic, and Costas A. Anastassiou

Supplementary Material

Parameters	Apical Dendrite	Basal Dendrite	Soma	Axon	Unit	Modfile
C_m	[0.5, 10]	[0.5, 10]	[0.5, 10]	[0.5, 10]	μFcm^{-2}	pas
g_{pas}	$[10^{-7}, 10^{-2}]$	$[10^{-7}, 10^{-2}]$	$[10^{-7}, 10^{-2}]$	$[10^{-7}, 10^{-2}]$	Scm^{-2}	pas
e_{pas}	[-120, -60]	[-120, -60]	[-120, -60]	[-120, -60]	mV	pas
R_a	[50, 200]	[50, 200]	[50, 200]	[50, 200]	Ωcm	pas
I_h	$[10^{-7}, 10^{-4}]$	$[10^{-7}, 10^{-4}]$	$[10^{-7}, 10^{-4}]$	-	Scm^{-2}	lh.mod
NaT	$[0, 10^{-1}]$	$[0, 10^{-2}]$	[0, 5]	-	Scm^{-2}	NaTs2_t.mod
NaT	-	-	-	[0, 10]	Scm^{-2}	NaTa_t.mod
NaP	-	-	[0, 1]	[0, 5]	Scm^{-2}	Nap_Et2.mod
NaV	-	$[10^{-7}, 10^{-1}]$	$[10^{-7}, 10^{-1}]$	$[10^{-7}, 5]$	Scm^{-2}	NaV.mod
KT	-	-	[0, 1]	[0, 1]	Scm^{-2}	K_Tst.mod
KP	-	-	[0, 1]	[0, 1]	Scm^{-2}	K_Pst.mod
$Kv3.1$	[0, 1]	[0, 1]	[0, 2]	[0, 2]	Scm^{-2}	Kv3_1.mod
$Kv2\text{-like}$	-	-	-	$[10^{-7}, 10^{-1}]$	Scm^{-2}	Kv2like.mod
I_m	$[10^{-7}, 10^{-2}]$	$[10^{-7}, 10^{-2}]$	-	-	Scm^{-2}	Im.mod
I_{mV2}	-	$[10^{-7}, 10^{-2}]$	-	-	Scm^{-2}	Im_v2.mod
SK	-	-	$[10^{-7}, 10^{-1}]$	$[10^{-7}, 10^{-1}]$	Scm^{-2}	SK.mod
Ca_{HVA}	-	-	$[10^{-7}, 10^{-3}]$	$[10^{-7}, 10^{-3}]$	Scm^{-2}	Ca_HVA.mod
Ca_{LVA}	-	-	$[10^{-7}, 10^{-2}]$	$[10^{-7}, 10^{-2}]$	Scm^{-2}	Ca_LVA.mod
$\gamma_{CaDynamic}$ s	-	-	$[5 \times 10^{-4}, 0.05]$	$[5 \times 10^{-4}, 0.05]$		CaDynamics.mo d
$decay_{CaDynamic}$ s	-	-	[20, 1000]	[20, 1000]	ms	CaDynamics.mo d

Table S1: Conductance density bounds for spiny/aspiny cells. Red and blue highlight across rows or columns represent specificity to excitatory (spiny) and inhibitory (aspiny) cells respectively. Note that none of the aspiny cell reconstructions in the Allen Cell-Types database has apical dendrite markings, thus the conductances on the apical dendrite in our models is specific to spiny cells.

Feature Name	eFEL Name	Type	Description
voltage_base	voltage_base	Numeric	The average voltage during the last 10% before stimulus onset in mV
steady_state_voltage	steady_state_voltage	Numeric	The average voltage after the stimulus
voltage_deflection	voltage_deflection _vb_sse	Numeric	The voltage deflection between voltage base and average voltage during the last 10% of the stimulus duration in mV.
sag_amplitude	sag_amplitude	Numeric	The difference between the minimal voltage and average voltage during the last 10% of the stimulus duration in mV.
sag_ratio	sag_ratio1	Numeric	The ratio between the sag amplitude and the maximal sag extend from voltage base.
decay_time_constant_after_stim	decay_time_constant _after_stim	Numeric	The decay time constant of the voltage right after the stimulus.
Spikecount	Spikecount	Numeric	Number of spikes in the trace, including outside of stimulus interval.
spike frequency	mean_frequency	Numeric	Mean frequency calculated as number of action potentials during stimulation divided by time between stimulus onset and last spike in Hz.
time_to_first_spike	time_to_first_spike	Numeric	Time to first spike in ms.
AP_amplitude	AP_amplitude_from _voltagebase	Numeric	Height at peak of action potential in mV from voltage base. Mean for all AP.
AP_width	AP_width	Numeric	Mean of width at -20 mV of AP in ms. Mean for all AP.
AHP_depth	AHP_depth	Numeric	Relative voltage values with respect to voltage_base at the first after-hyperpolarization. Mean for all AP.
adaptation_index2	adaptation_index2	Numeric	Normalized average difference of two consecutive ISI starting from second ISI.

ISI_CV	ISI_CV	Boolean	The coefficient of variation of the ISI.
depolarization_block	depol_block	Boolean	True if depolarization block is detected during spiking.
check_AISInitiation	check_AISInitiation	Boolean	True if time difference between same AP recorded at axon and soma is positive False otherwise

Table S2: Ephys features used at different stages during model generation workflow. sag_ratio1 is not used in the optimization but used in the comparison between Nr5a1 and Rbp4 Cre-lines in Figure 6 of the main manuscript.

Stage	Parameters	Frozen Parameters/Tolerance	eFEL Features	Stimulus
Stage 0	<ul style="list-style-type: none"> c_m e_{pas} g_{pas} R_a 	–, –	<ul style="list-style-type: none"> voltage_base steady_state_voltage voltage_deflection_vb_sse decay_time_constant_after_stim 	All depolarizing subthreshold
Stage 1	<ul style="list-style-type: none"> \bar{g}_{lh} 	None, $\pm 50\%$	eFEL Features at Stage 0+ <ul style="list-style-type: none"> sag_amplitude 	All depolarizing subthreshold + all hyperpolarizing subthreshold
Stage 2	<ul style="list-style-type: none"> \bar{g}_{NaT}, \bar{g}_{NaP} \bar{g}_{NaV} \bar{g}_{KT}, \bar{g}_{KP} $\bar{g}_{Kv3.1}$ $\bar{g}_{Kv2like}$ \bar{g}_{Im}, \bar{g}_{Imv2} \bar{g}_{SK} gamma_decay_CaDynamics 	None, $\pm 50\%$	<ul style="list-style-type: none"> voltage_base steady_state_voltage mean_frequency Spikecount time_to_first_spike AP_amplitude_from_voltagebase AP_width AHP_depth adaptation_index2 ISI_CV depol_block check_AISInitiation 	$\times 2$ spiking traces with maximal amplitude + Rheobase trace + Maximal subthreshold

Table S3: Details of Optimization Workflow: We fit conductance densities (\bar{g}) on the primary neurites-apical, basal dendrites, soma and axon, with the assumption that these conductances are distributed uniformly across each section of the reconstructed morphology belonging to the neurite.

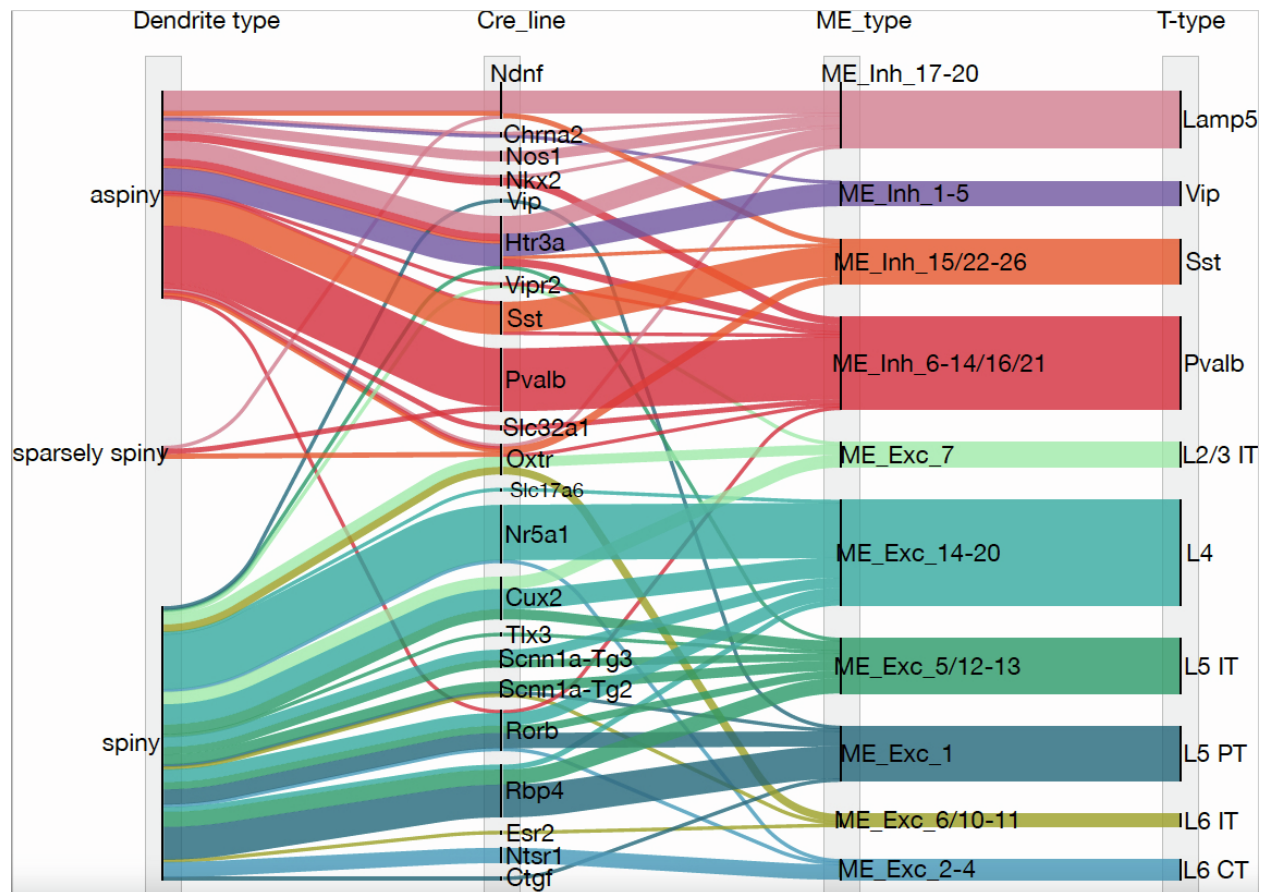


Figure S1: Taxonomies represented in the data used to generate the single cell models, Related to Figure 1. Four major cellular taxonomies are considered (left-to-right): morphological, Cre line-specific, morphoelectric (ME) and transcriptomic. Three morphological types are considered: aspiny, sparsely spiny and aspiny based on (Gouwens et al., 2019). Transgenic Cre lines crossed to Cre-reporter lines were used to genetically target specific groups of cells. The morphoelectric taxonomy is based on morphological as well as cellular electrophysiology properties following the analysis in (Gouwens et al., 2019). Finally, the transcriptomic taxonomy is based on the transcriptomic profiles of single-cells where expression of each gene is quantified as counts over million reads (Tasic et al., 2016, 2018a).

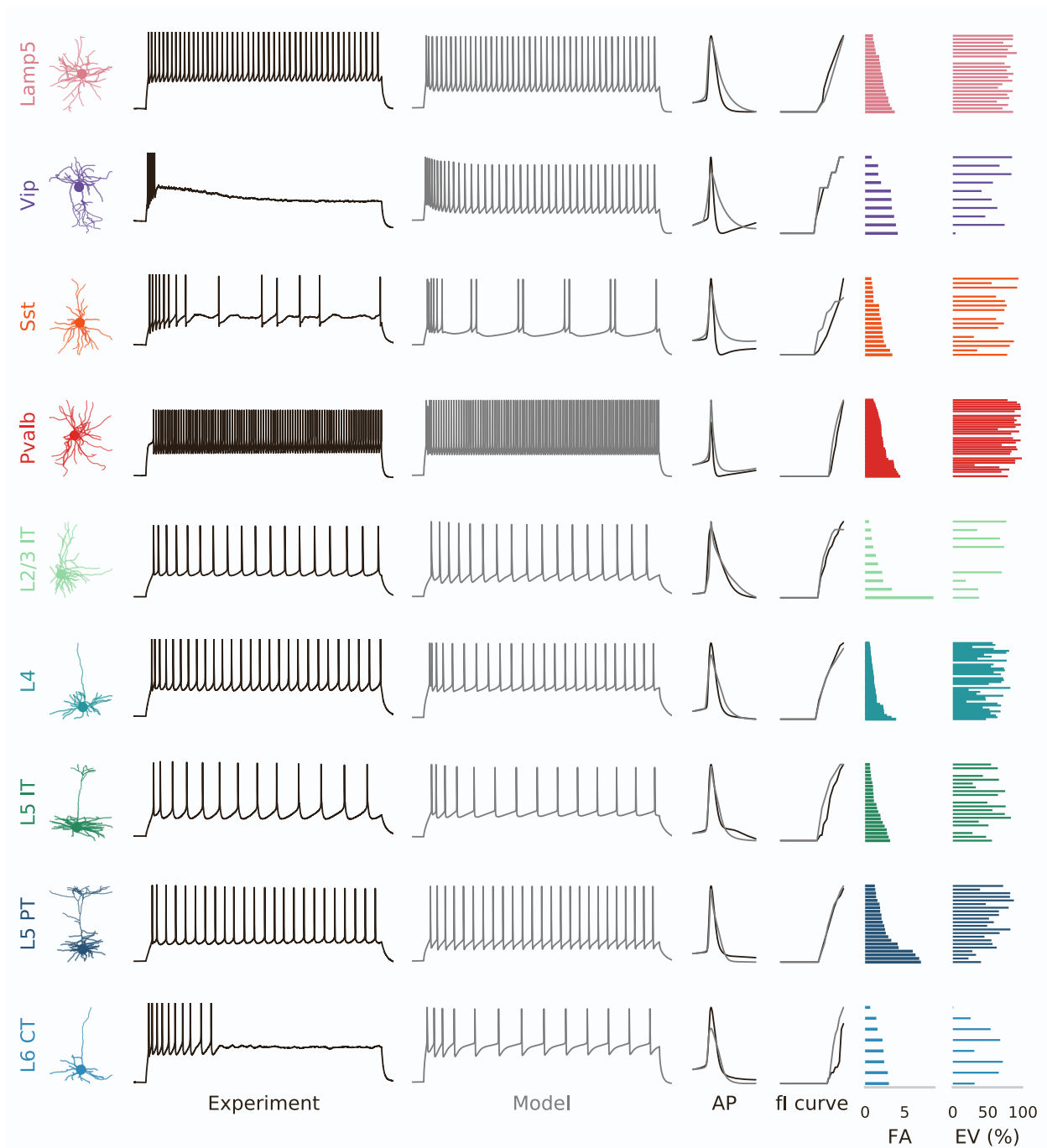


Figure S2: Performance of representative single cell models across transcriptomic types, Related to Figure 1. From left to right, transcriptomic subclasses (only subclasses with at least 5 models are selected), morphology, experimental and model suprathreshold response, spike shape and fI curves are illustrated. The last two columns in the grid show the feature average (FA) at training and explained variance (EV) under colored noise stimulus. The representative model belongs to the cell located at the median of the feature average distribution of the member t-types.

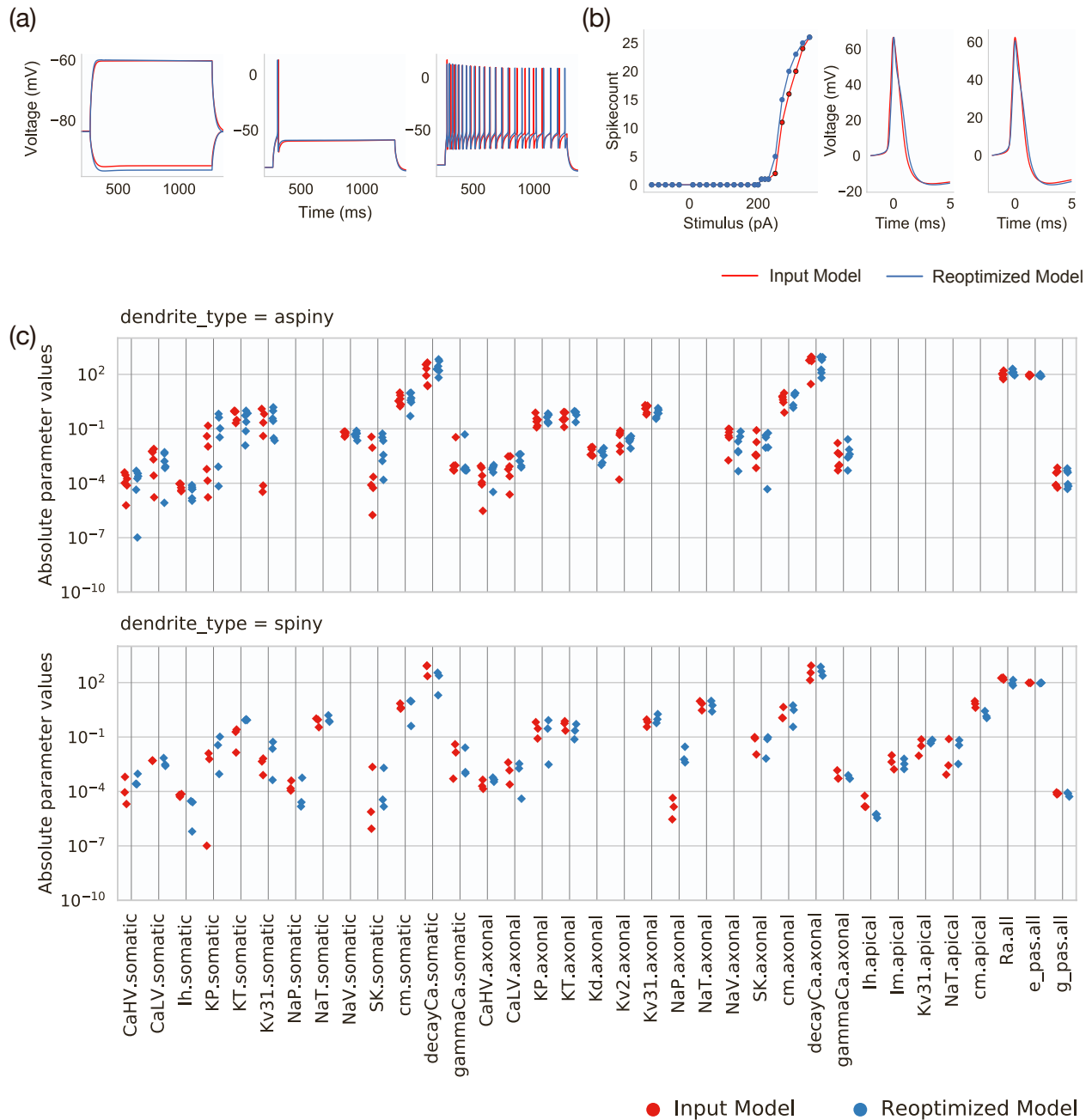


Figure S3: Convergence of the optimization workflow for a ground truth solution, Related to Figure 1. The simulated response from the all-active model (CellID: 468193142) is fed to the workflow for a second round of model generation. This allows comparing the conductance vector of the starting model with the re-optimized model. **(a)** Comparison between subthreshold and suprathreshold responses (input model: red; re-optimized model: blue). **(b)** f-I curve and action potential waveforms for the input and re-optimized model. **(c)** Scatter plot (top: 6 aspiny neurons – 2 each from Vip, Sst, Pvalb subclass, bottom: 3 spiny or excitatory neurons) of the original model (fitted from experimental ephys recording) parameters overlaid with the re-optimized model (fitted from the simulation of the original model) parameters. Note that the majority of the conductance parameters exhibit convergence to their ground truth value indicating the efficacy of the optimization workflow.

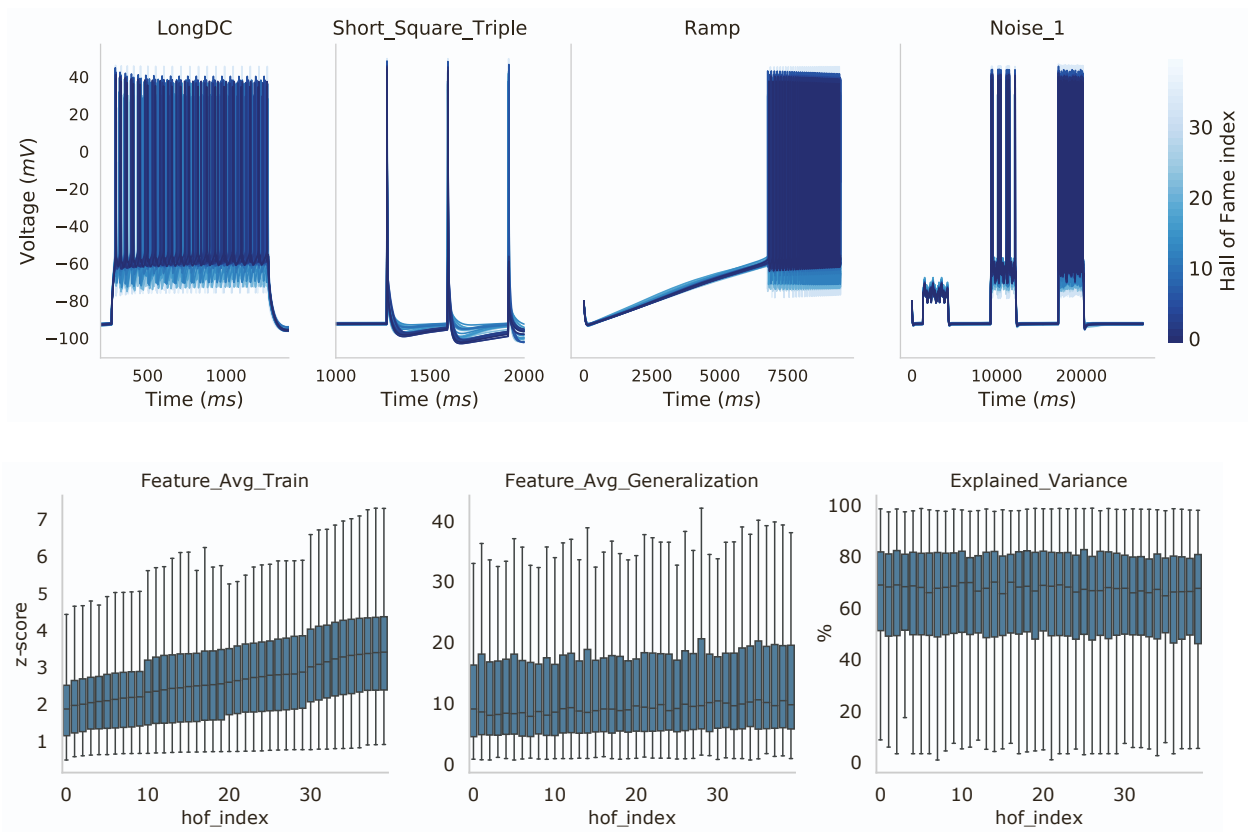


Figure S4: Training and generalization of hall-of-fame (hof) models, Related to Figure 1-2. (a) 40 hall of fame (hof) models are generated for each cell. (Left to right): response of hof models to 1s dc stimulus, short square triple pulse stimuli, ramp and noise stimulus. A number of E-features is extracted from the various stimuli (Table S2). (b) Feature average (computed in terms of z-score) and explained variance shown for 230 cells against the hof index (sorted according to training error of each cell). While the feature average exhibits an increasing trend (increasing error with hof index), explained variance (to untrained stimuli) is comparable across hof indices.

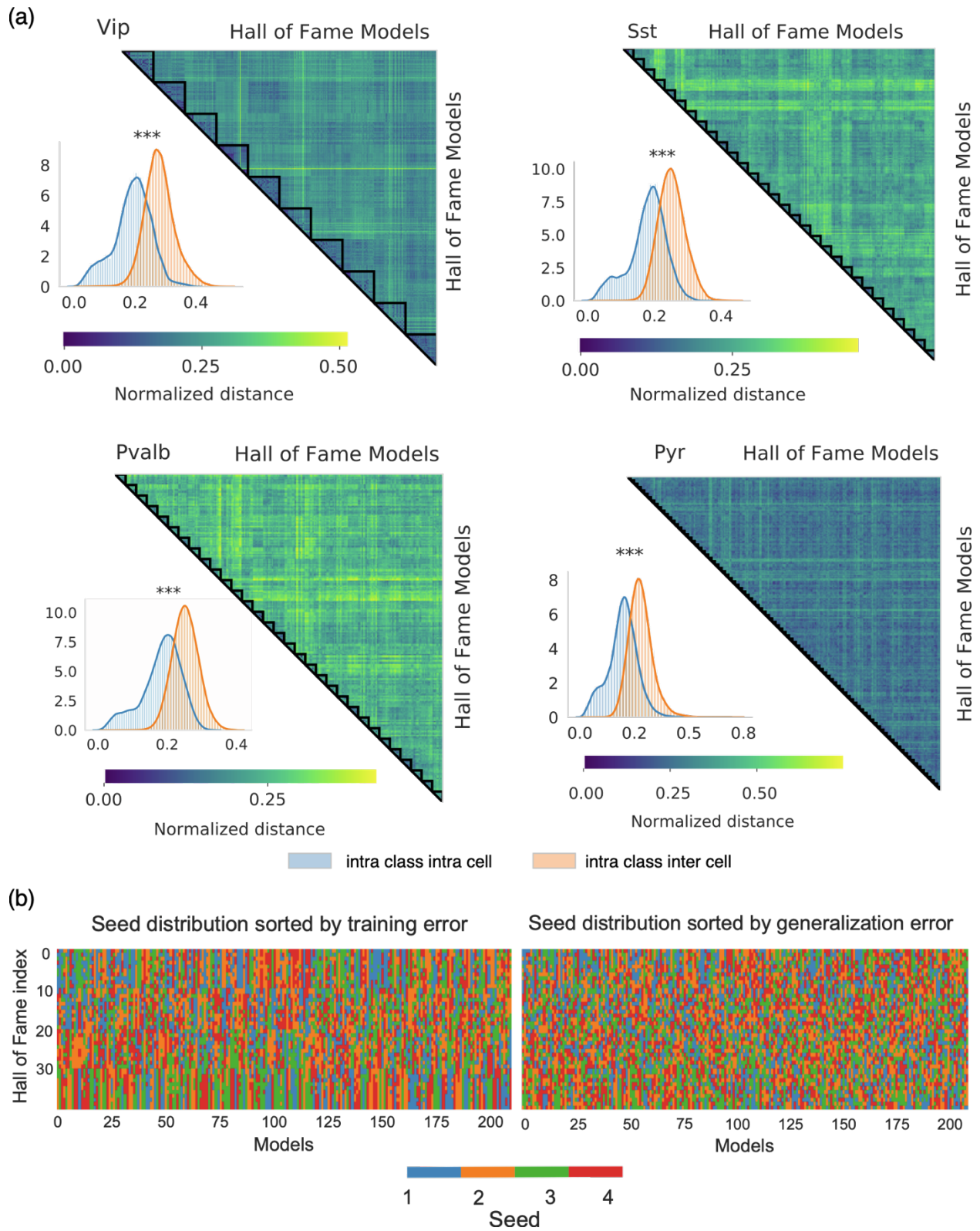


Figure S5: Parameter diversity across cortical cell classes, Related to Figure 2. (a) Similar to Figure 2b, the dispersion matrix for the hall of fame parameters within and across cell for the 4 broad subclasses. The block diagonals for 'Pyr' are compressed due to numerical advantage in comparison to

the other inhibitory subclasses. For each broad subclass the intra-class intra-cell dispersion (blue) is less than intra-class inter-cell (orange). Mann-Whitney U-test; Statistical significance: *: p-val < 0.05, **: p-val < 10^{-2} , ***: p-val < 10^{-3} . **(b)** The hof models for each cell is not dependent on the initialization. The single-color strands belonging to one seed when sorted to training error (left) is lost when the models are arranged according to the generalization error, i.e., performance on unseen stimulus set. This points to an existence of attraction basin for this highly constrained optimization formulation.

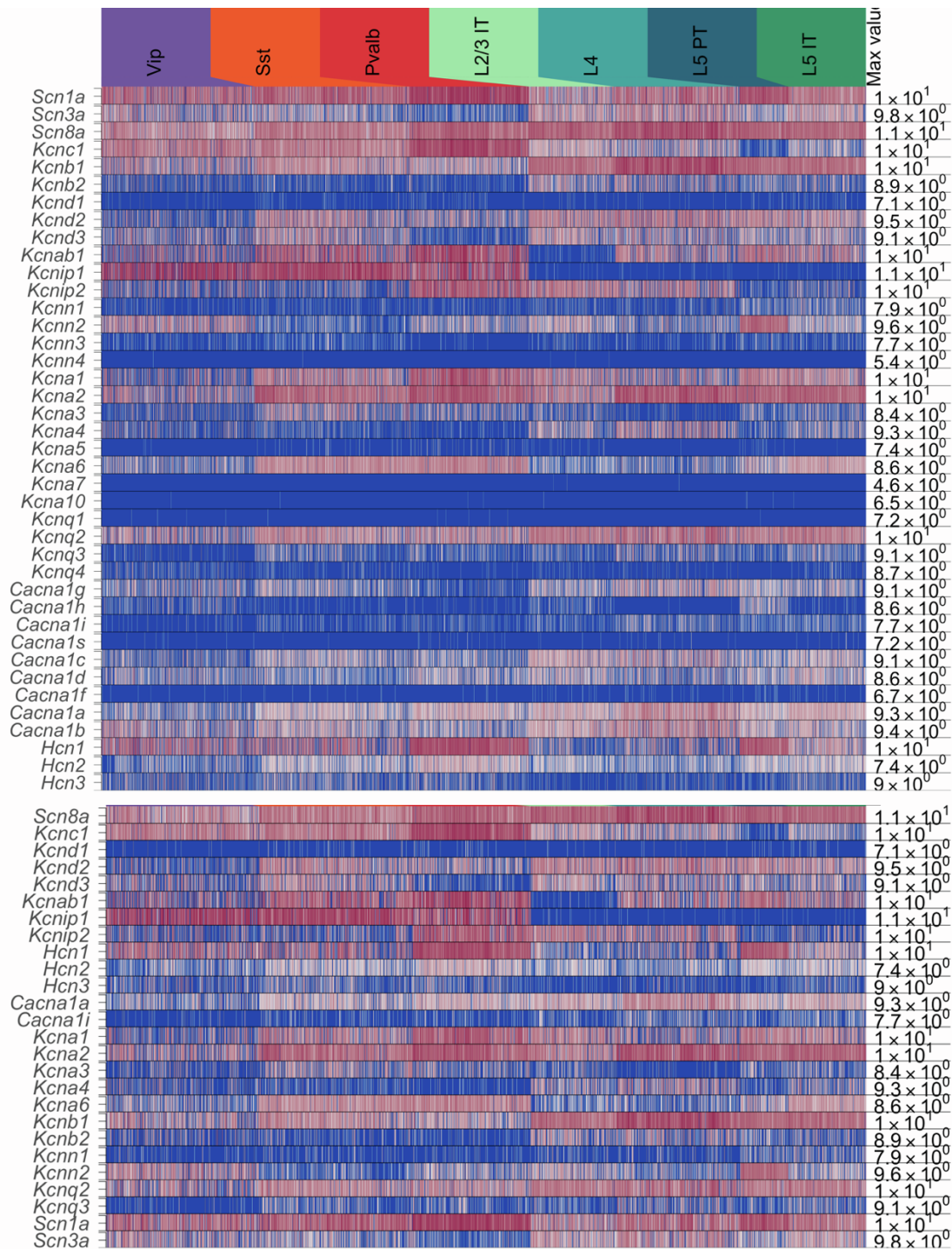


Figure S6. Differentially expressed genes revealed via modeling, Related to Figure 3. (Top) All statistically significant differentially expressed genes that encode ion conductances. **(Bottom)** Subset of the ionic conductance genes revealed via pairwise comparison of conductance density in the all-active models for the 7 transcriptomic subclasses.

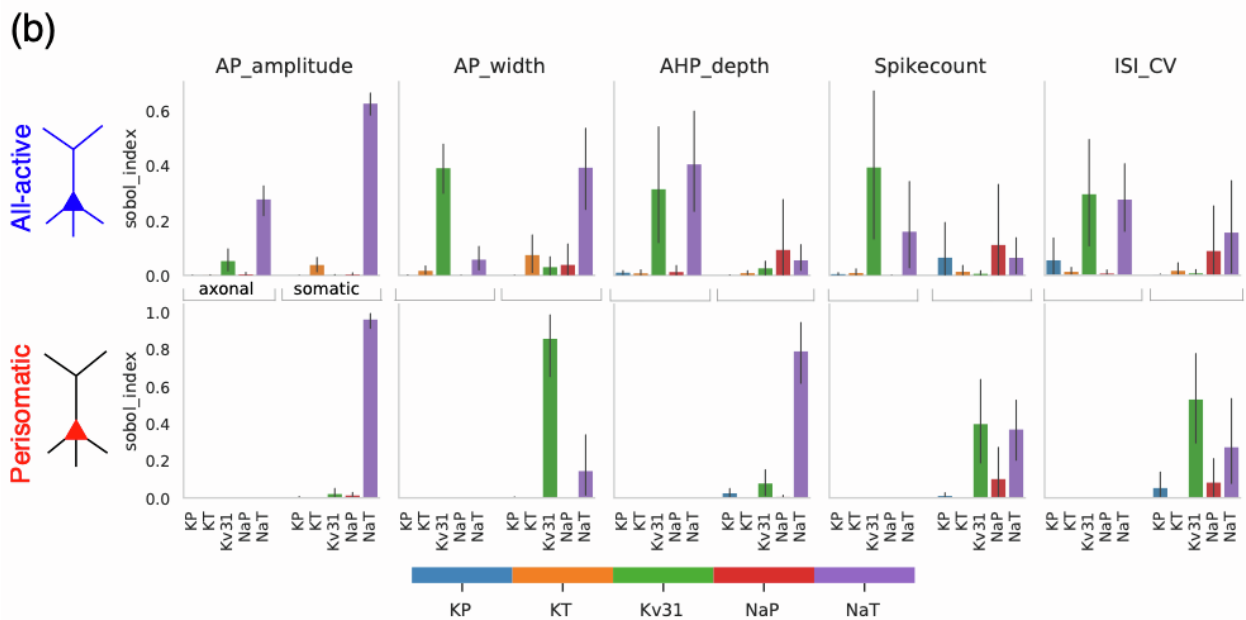
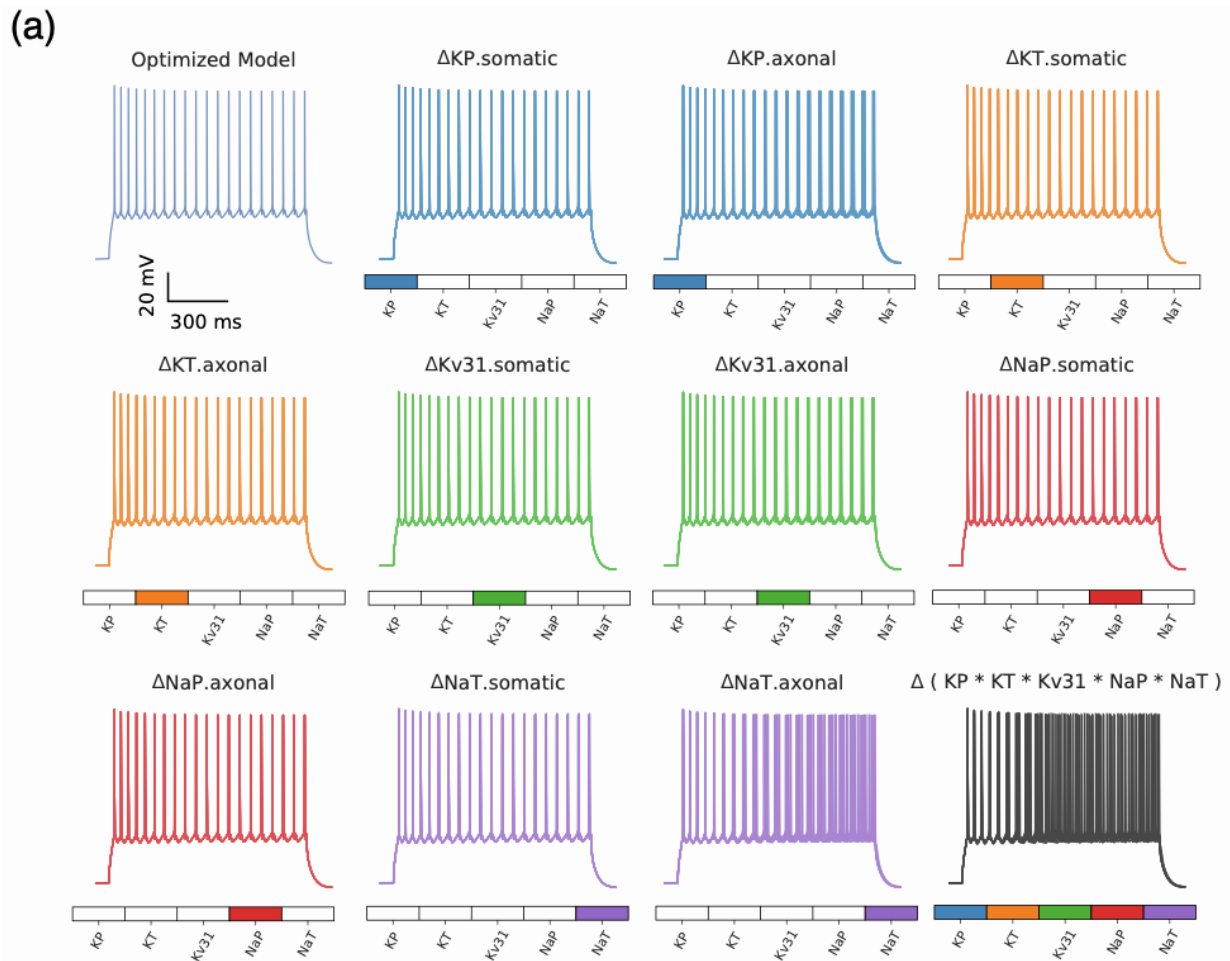


Figure S7: Illustration of the sensitivity analysis and its utility in revealing mechanistic differences between all-active and perisomatic models, Related to Figure 3. (a) (top left) Output of the best model (least training error, i.e., hof index = 0) for Cell ID: 483101699 at 1s long stimulus of amplitude 270pA. In the following panels 100 simulations are shown for the same protocol with each of the selected K^+ , Na^+ channel groups (indicated by the color bar at the bottom of each panel) individually perturbed within a $\pm 10\%$ tolerance level about the optimized value. Finally, at bottom right the channels are perturbed together, equivalent to the sobol analysis computations and plot the simulations for 100 such parameter combinations. Only the parameters on the color bar are modified in the illustration, the rest of the channel densities remain unperturbed from their optimized value. **(b)** The comparison between the sobol indices as it relates to spike amplitude, width, AHP depth, spike count and ISI coefficient-of-variation for all-active and perisomatic models (10 excitatory cells each, bar: mean; error bar: std). Note the absence (due to the design of perisomatic models) of axonal conductances in the bottom panel, which play a key role for the all-active spiking features (top).

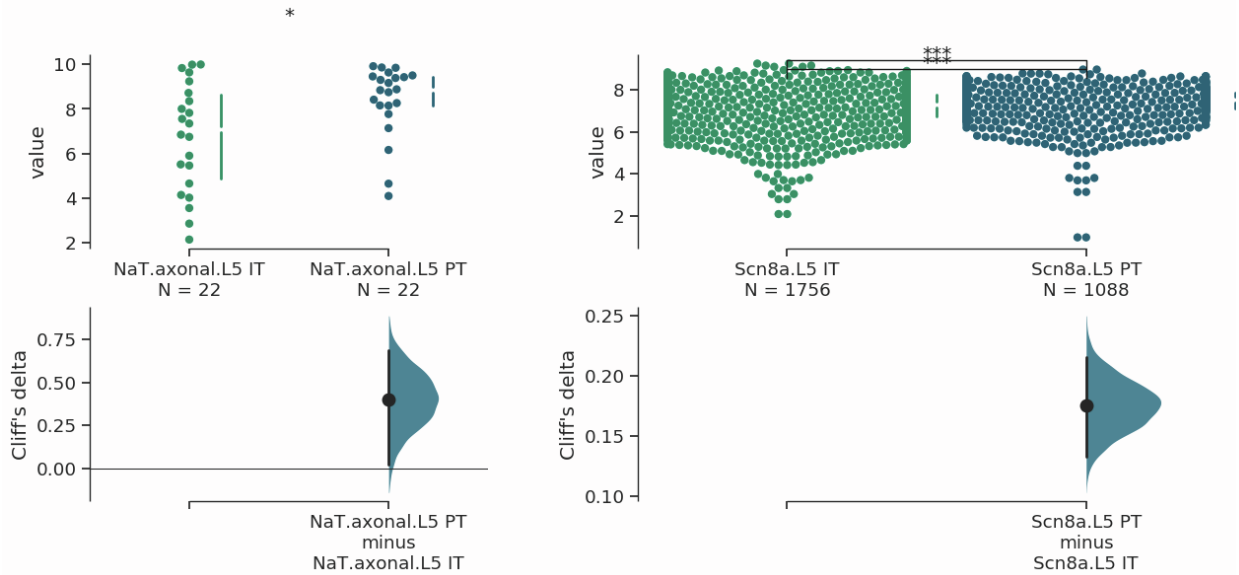


Figure S8: Statistically significant difference in the axonal NaT conductance between L5 IT and PT models, Related to Figure 4. In the analysis presented in Figure 4 (main manuscript), pairwise comparison between L5 IT and PT all-active models reveals, beyond an elevated somatic and apical h channel, also a transient axonal Na conductance density for L5 PT cells (with the same Hcn1, Scn8a expression pattern between the two classes). Results for the h channel comparison are presented in Figure 4 (main manuscript). **(Top left)** Pairwise comparison in the transient axonal Na conductance between L5 IT and PT all-active models ($p\text{-val} < 0.05$, one-sided Mann-Whitney U-test). **(Bottom left)** Cliff's delta effect size analysis of the medians of the data above (Ho et al., 2019)). **(Top right)** Comparison for gene expression of Scn8a from the single-cell RNA sequencing data between L5 IT and PT is compatible with model prediction, i.e. L5 PT cells exhibits elevated Scn8a expression compared to L5 IT cells. **(Bottom right)** Cliff's delta effect size analysis of the medians for Scn8a expression. Note the agreement both in terms of statistical significance as well as the effect direction supported by both modalities (L5 PT > L5 IT).

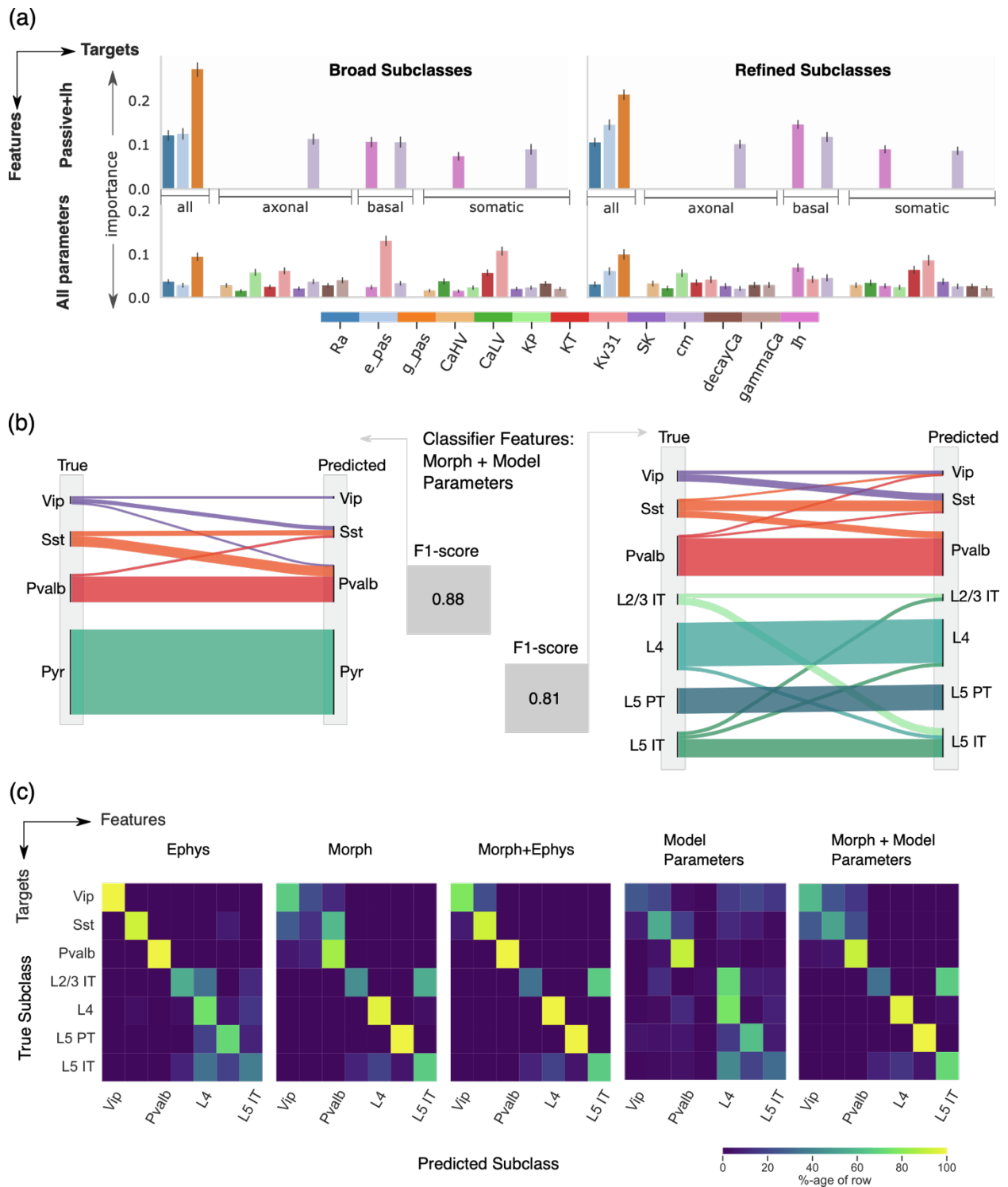


Figure S9: Ion channel conductance specificity along the morphology of all-active models informs of cell-type subclasses, Related to Figure 6. (a) Random forest classifier trained on model parameters for broad and refined cell-type subclasses. Classifier (top) trained only on passive and h-channel parameters and (bottom) the full set of conductances. Features are sorted according to the parent section of the morphology ('all'- common to the entire morphology, axonal, apical, basal, somatic) and same color

is used to indicate a parameter across sections. Among the passive properties (top) g_{pas} holds the highest importance whereas within the entire parameter set (bottom) Kv3.1 is dominant. Note that going into the full feature set, g_{pas} retains relative influence in the classifier across targets. **(b)** Sankey diagrams showing the tendencies for classifiers constructed out of Morph+Model parameters for the two targets on the test set. (Left) For broad subclasses Pyr and Pvalb categories are well separated with Sst and Vip cells misclassified. (Right) For the transcriptomic subclasses, except for Vip cells, the classifier is able to delineate cell-types across excitatory and inhibitory classes. **(c)** Confusion matrices for the Random Forest classifier trained on different sets of features (columns) for predicting transcriptomic subclasses (F1-score on the test set: 0.76, 0.75, 0.88, 0.59 and 0.81 respectively).

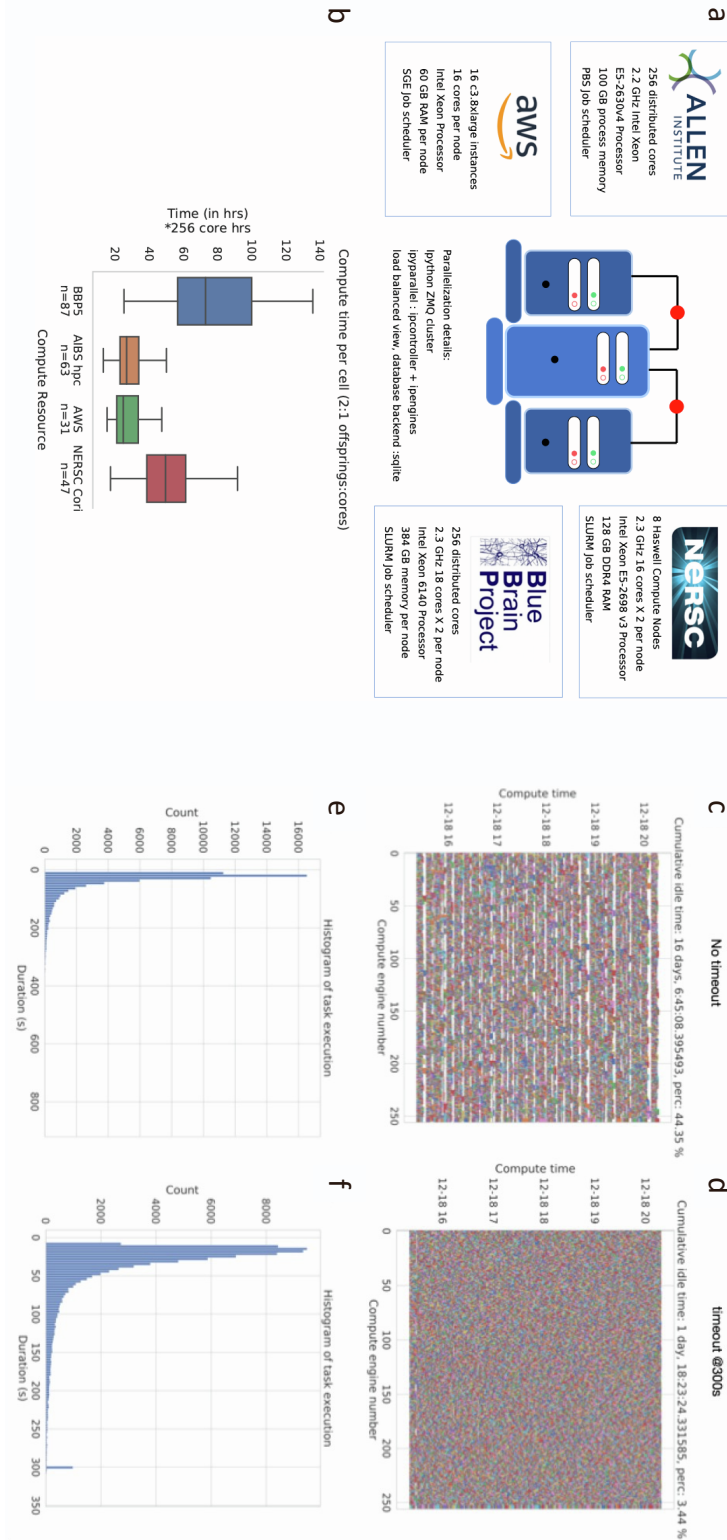


Figure S10: Computational resources employed during the model generation workflow, Related to Figure 1-2. (a) Resources utilized include the in-house Allen Institute for Brain Science High Performance Computing (AIBS hpc) cluster, Amazon Web Services (AWS) EC2 instances in conjunction with Wasabi cloud storage as AWS S3 substitute, Cori supercomputers at National Energy Research Scientific

Computing Center (NERSC) and Supercomputing infrastructure at Blue Brain Project (BBP5), École Polytechnique Fédérale de Lausanne, Switzerland. In total close to 3.5 million core hours are utilized across these four Linux based systems for the ~230 models. **(b)** Reduction in compute time and subsequently core hours in AIBS hpc and AWS EC2 instances is mainly due to an algorithmic improvement in the latter stages of the model generation timeline, where solutions were discarded for which evaluation exceeded a 300s cut-off. Number of requested cores at each job is equal across. **(c-f)** Effect of adding timeout functionality within BluePyOpt. **(c)** Without timeout the evolutionary algorithm occasionally encounters a parameter combination resulting in a stiff differential equation. The blank spaces represent the idle time for the rest of engines in a distributed infrastructure. **(d)** The histogram of the task execution shows that the evaluation time for rare individuals go up to 900s. **(e)** In comparison adding a timeout of 300s enables us to run a controlled optimization in the HPC clusters with drastic reduction in idle time (44% to 3%). The jump in the histogram **(f)** at 300s means that the engines are reassigned to evaluate new individuals without completing the numerical integration when the cut-off time is hit. For this illustration we have used the stage 2 for model generation of CellID: 483101699 under identical parameter bounds.